2013

Inertial oscillations in the Gulf of Mexico during 2005 hurricane season

Fan Zhang
Louisiana State University and Agricultural and Mechanical College

INERTIAL OSCILLATIONS IN THE GULF OF MEXICO DURING 2005 HURRICANE SEASON

A Thesis

Submitted to the Graduate Faculty of the
Louisiana State University and
Agricultural and Mechanical College
in partial fulfillment of the
requirements for the degree of
Master of Science

in

The Department of Oceanography and Coastal Sciences

by
Fan Zhang
B.S., Nanjing University, 2007
August 2013

Acknowledgements

I wish to express my gratitude to my advisor Dr. Chunyan Li for his patience, kindness and guidance during my master study. The constructive suggestions from Dr. Lawrence Rouse, Dr. Kanchan Maiti and Dr. Nan Walker are also appreciated. Thanks also go to Nabi, Chenguang, Chet and Jun for their helpful discussion on my thesis. The CSI Mooring Data is from Drs. Masamichi Inoue and Susan Welsh supported by from the Bureau of Ocean Energy Management, Regulation and Enforcement (BOEMRE).

Table of Contents

List of Tables

List of Figures

Abstract

Near Inertial Oscillations (NIOs) are widely observed in ocean current data after severe weather. In this work, we analyzed the NIOs in the Central Gulf of Mexico (GoM) associated with 6 hurricanes/tropical storms in 2005, including Katrina and Rita, based on the deep ocean mooring from Coastal Studies Institute (CSI), LSU. The basic characteristics of the NIOs, such as phase speed, group speed, frequency, energy were discussed. The phase speed ranged from 0.56 cm/s to 2 cm/s above the thermocline for the NIOs during Hurricane Katrina and Rita, while the group velocity varied from 0.047 cm/s above the thermocline to 0.25 cm/s below it for the NIOs during Hurricane Karina. The theory of NIO frequency: $f_{eff} = f + \zeta/2$ were examined with Sea Surface Height (SSH) data, and a correlation between the real and theoretical frequencies was established (R^2=0.32). A comparison between the strength of Loop Current (LC) and NIOs induced by severe hurricanes was also made. The result shows that the LC could have comparable instant high energy as severe hurricane induced NIOs, while the impact of a strong LC could last longer.

1. Introduction

The Gulf of Mexico (GoM) is located at the southeast of North American. It is called the "American Mediterranean". It is surrounded by Florida, Alabama, Mississippi, Louisiana and Texas of the U.S., Tamaulipas, Veracruz, Tabasco, Campeche and Yucatan of the Mexico and the island of Cuba (Gore, 1992). The latitude range of GoM is from around 20^{o}N to around 30^{o}N. Because of its relative low latitude, the GoM is frequently affected by tropical storms and hurricanes.

As an example, between June 1, 2005 and Nov. 10, 2005, there were 6 hurricanes and tropical storms passing the central GoM, within a 350 km range of a deep ocean mooring (25.5^{o}N, 87^{o}W) (Welsh et al., 2009). Among these events, Hurricanes Katrina and Rita were the closest which brought dramatic influence of the atmosphere onto the ocean. Their effects were well recorded by the mooring instruments; and we found intensive near inertial oscillations (NIOs) in the mooring data during these hurricane time periods. Though NIOs were widely observed after the passage of storms in the literature (e.g., Alford, 2006; Gill, 1982; Gill, 1984; Kundu and Thomson, 1985; Meyers, 2008; Stockwell et al., 2004; Sun et al., 2011; Wang, 1991), and characteristics of NIOs have been extensively discussed (e.g., Fu, 1981; Gill, 1982; Pinkel, 2007; Shearman, 2005; Young and Jelloul, 1997; Young and Balmforth, 1999), the research of the variations of their spectrum with time and depth using mooring data were hardly found. However, the data from this deep ocean mooring provided us the opportunity to explore the variations of NIOs spectrum as a function of depth and time. On the other hand, because the mooring is so close to the center of Katrina and once within 30 km (Welsh et al., 2009), it made the discussion of variation of hurricane-wind generated NIO energy meaningful. The NIOs are also believed to be one of the important factors in the vertical mixing, which could be associated with the enhancement of particulate organic carbon export flux and the increased biological activity after severe weather (Hung et al., 2009).

2. Literature Review

2.1 Characteristics of Ideal Inertial Oscillation

Inertial Oscillation in the ocean is a motion caused by the rotation of the earth (Coriolis force). A sudden wind force will tend to push the surface water moving in the direction of wind but then turn to the right hand side of the wind direction in northern hemisphere because of the Coriolis effect. Once the motion is setup, the surface water will continue moving in a circle. If there is no more external forces, i.e. no friction and if furtehr, there is no advectional effect (linear approximation), the rotation will be described by Equ. 2-1, where *t* is time, *u* and *v* are the velocity components in the east and north directions, respectively, *f* is the Coriolis parameter:

$$\begin{cases} \dfrac{\partial u}{\partial t} = fv \\ \dfrac{\partial v}{\partial t} = -fu \end{cases} \tag{2-1}$$

The solution to this equation is:

$$\begin{cases} u = A\sin(ft + \varphi_0) \\ v = A\cos(ft + \varphi_0) \end{cases} \tag{2-2}$$

For convenience, let's assume that the initial phase φ_0=0, then:

$$\begin{cases} u = A\sin(ft) \\ v = A\cos(ft) \end{cases} \tag{2-3}$$

This rotation motion is identified as inertial oscillation, where the word "inertial" refers to the effect of the inertial force (Coriolis force) induced by the rotation of the reference frame—the earth and the word "oscillation" is used because the water particle will rotate in a circle. From Equ.2-3 we can see that the inertial oscillation is a circular motion; the frequency of inertial motion is the Coriolis parameter *f*; the *u*, *v* components have the same amplitudes (thus a circular, rather than an elliptic or linear, motion); there is a 90 degree phase difference between *u* and *v* and an inertial oscillation in the northern (southern) hemisphere rotates clockwise (counterclockwise).

2.2 Wind Forced Inertial Oscillation

Another situation is when the wind continues its direction and magnitude for a long time, which will require the inclusion of wind stress into the equation of motion (Gill, 1982):

$$\begin{cases} \frac{\partial \mathrm{u}}{\partial \mathrm{t}} - \mathrm{fv} = -\frac{1}{\rho}\frac{\partial \mathrm{p}'}{\partial \mathrm{x}} + \frac{1}{\rho}\frac{\partial \mathrm{X}}{\partial \mathrm{z}} \\ \frac{\partial \mathrm{v}}{\partial \mathrm{t}} + \mathrm{fu} = -\frac{1}{\rho}\frac{\partial \mathrm{p}'}{\partial \mathrm{x}} + \frac{1}{\rho}\frac{\partial \mathrm{Y}}{\partial \mathrm{z}} \end{cases} \quad (2-4)$$

Equ.2-4 is the equation of motion, including Coriolis force, pressure gradient and wind shear force, where ρ is the density of seawater (we assume that density is constant with time and depth for convenience), p' is the pressure, X is the horizontal stress in the x direction and Y is the horizontal stress in the y direction. Gill (1982) indicated that we could separate Equ.2-4 into the shear force part and the pressure gradient part because the equation is linear. The pressure gradient balances with the geostrophic flow and the shear force part is related to a forced inertial oscillation. Since inertial oscillation is our concern, we only look at the shear force part:

$$\begin{cases} \frac{\partial u_s}{\partial t} - f v_s = \frac{1}{\rho}\frac{\partial X}{\partial z} \\ \frac{\partial v_s}{\partial t} + f u_s = \frac{1}{\rho}\frac{\partial Y}{\partial z} \end{cases} \quad (2-5)$$

Where u_s, v_s is the velocity generated by shear force. If we integrate Equ.2-5 with depth z on both sides, we can get:

$$\begin{cases} \rho\left(\frac{\partial U}{\partial t} - fV\right) = X \\ \rho\left(\frac{\partial V}{\partial t} + fU\right) = Y \end{cases} \quad (2-6)$$

Where U and V represent the volume transport integrated for the entire water column along x and y directions, respectively. Multiply the second equation of Equ.2-6 with the imaginary unit "i", and add both together, we can get:

$$\rho\left(\frac{\partial U}{\partial t} + i\frac{\partial V}{\partial t}\right) + if(U + iV) = X + iY \quad (2-7)$$

A solution to Equ.2-7 is:

$$U + iV = \frac{-i(X + iY)}{\rho f}(1 - e^{-ift}) \tag{2-8}$$

Using Euler Equation expanding the right side, we will get:

$$U + iV = \frac{1}{\rho f}[(Y - Y\cos(ft) + X\sin(ft)) + i(-X + X\cos(ft) + Y\sin(ft))] \tag{2-9}$$

Let $Y=a*\cos\beta$, $X=a*\sin\beta$, where $a^2=X^2+Y^2$ is the total horizontal shear, β is the angle from north to the wind direction. Then:

$$\begin{aligned} U + iV &= \frac{1}{\rho f}\big[(a * \cos\beta - a * \cos\beta * \cos(ft) + a * \sin\beta * \sin(ft)) \\ &+ i(-a * \sin\beta + a * \sin\beta * \cos(ft) + a * \cos\beta * \sin(ft))\big] \\ &= \frac{a}{\rho f}[(\cos\beta - \cos(ft + \beta)) + i(-\sin\beta + \sin(ft + \beta))] \end{aligned} \tag{2-10}$$

Comparing the real part and imaginary part of both sides of Equ.2-10, we can get:

$$\begin{cases} U = \dfrac{a}{\rho f}(\cos\beta - \cos(ft + \beta)) \\ V = \dfrac{a}{\rho f}(-\sin\beta + \sin(ft + \beta)) \end{cases} \tag{2-11}$$

We find that U and V consist of a constant flow:

$$\begin{cases} U_{constant} = \dfrac{a}{\rho f}\cos\beta \\ V_{constant} = -\dfrac{a}{\rho f}\sin\beta \end{cases} \tag{2-12}$$

and an inertial oscillation:

$$\begin{cases} U_{inertial} = -\dfrac{a}{\rho f}\cos(ft + \beta) \\ V_{inertial} = \dfrac{a}{\rho f}\sin(ft + \beta) \end{cases} \tag{2-13}$$

The Equ.2-12 showed that the direction of the constant flow is to the right (left) side of the horizontal wind stress in the northern (southern) hemisphere with a positive (negative) f. If we integrate the equations (2-11)

over time, only the constant flow will remain. This gives the direction of net volume transport to the right (left) of the wind in the northern (southern) hemisphere.

Equ.2-13 indicates that the amplitude of the constant wind forced inertial flow is proportional to the wind generated horizontal shear and inversely proportional to the local Coriolis parameter. If the wind is strong, we will have a strong inertial oscillation; if the latitude $\varphi \to 0$, $f=2\Omega*\sin\varphi \to 0$ (Ω is the angular velocity of the earth), U_{inertial} and V_{inertial} will be very large. Since U and V are integrations of velocity with depths and the magnitudes of U and V are determined by the wind stress for a specific area, if the depth is very shallow, then u_s and v_s will be a large number. This is the case for summer and autumn when the mixed layer is relatively thin (Gill, 1982).

An intuitive way to identify inertial oscillation from the current is to see the progressive vector of the water particle. A progressive vector (X, Y) is a time integration of the velocity vector (U, V) of a specific point as following:

$$\begin{aligned} \int Udt &= \int \frac{a}{\rho f}(\cos\beta - \cos(ft+\beta)) \\ \int Vdt &= \int \frac{a}{\rho f}(-\sin\beta + \sin(ft+\beta)) \end{aligned} \tag{2-14}$$

If the wind is southerly, $\beta = 0$:

$$\begin{aligned} \int Udt &= \int \frac{a}{\rho f}(1-\cos(ft))dt \\ \int Vdt &= \int \frac{a}{\rho f}\sin(ft)\,dt \end{aligned} \tag{2-15}$$

$$\begin{cases} X = \dfrac{a}{\rho f^2}(ft - \sin(ft)) + A \\ Y = -\dfrac{a}{\rho f^2}\cos(ft) + B \end{cases} \tag{2-16}$$

in which A and B are constants. If $A=B=0$, $\frac{a}{\rho f^2} = 1$, f(at 30^0N)$=2\Omega*\sin(30^0)=7.27*10^{-5}$, a five-day progressive vector is shown in Fig. 2-1, which is a typical trajectory of cycloid.

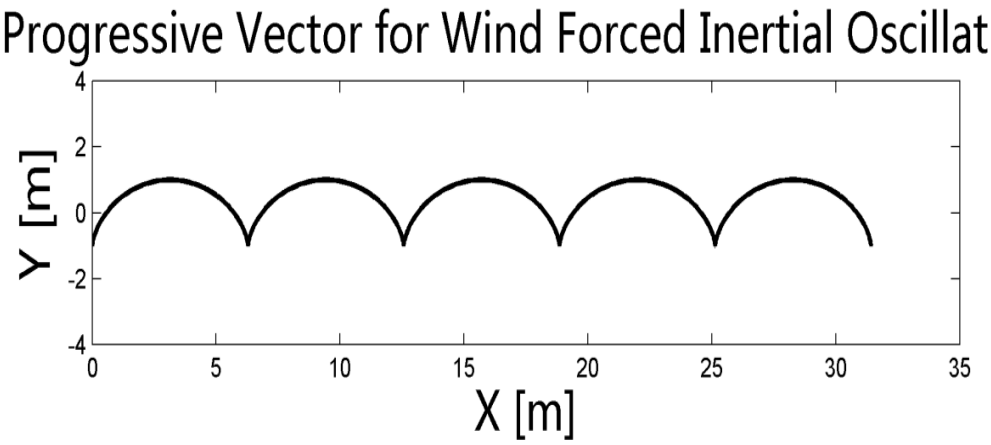

Figure 2-1 Progressive Vector for Wind Forced Inertial Oscillation

2.3 Inertial Oscillation and Internal Waves

Inertial oscillation generated by local wind explains the high peak in the near inertial frequency range in a power spectrum (Eckart, 1961; Fu, 1981; Garrett, 2000). The inertial frequency *f* is believed to be the lower bound of internal waves which can propagate freely based on the internal wave frequency dispersion relationship:

Supposing waves to be sinusoidal in time, at frequency ω:

$$w \sim e^{i\omega t} \tag{2-17}$$

In which, *w* is the vertical velocity and ω is the fixed frequency in an Eulerian Frame.

The usual approach to derive the frequency dispersion relationship is solving Equ.2-18 (Vanderhoff *et al*., 2008):

$$\begin{cases} \dfrac{\partial u}{\partial t} - fv = -\dfrac{\partial p}{\partial x} \\ \dfrac{\partial v}{\partial t} + fu = -\dfrac{\partial p}{\partial y} \\ \dfrac{\partial w}{\partial t} = -\dfrac{\partial p}{\partial z} - b \\ \dfrac{\partial u}{\partial x} + \dfrac{\partial v}{\partial y} + \dfrac{\partial w}{\partial z} = 0 \\ \dfrac{\partial b}{\partial t} - N^2 w = 0 \end{cases} \tag{2-18}$$

In which, N is the time-averaged buoyancy frequency. One solution to Equ.2-18 is:

$$\omega^2 = f^2 \frac{{k_z}^2}{{k_x}^2+{k_y}^2+{k_z}^2} + N^2 \frac{{k_x}^2+{k_y}^2}{{k_x}^2+{k_y}^2+{k_z}^2} \qquad (2-19)$$

This solution denotes that the range of ω is from f to N, which means that the lower bound of freely propagating internal wave frequency should be f.

Kunze (1985) suggested that since near inertial oscillation and geostrophic flow had similar horizontal scale, the two advection terms of the momentum equations $U\frac{\partial u}{\partial \mathrm{x}} + V\frac{\partial v}{\partial y} + W\frac{\partial w}{\partial \mathrm{z}}$ and $u\frac{\partial U}{\partial \mathrm{x}} + v\frac{\partial V}{\partial y} + w\frac{\partial W}{\partial \mathrm{z}}$ should be retained in Equ.2-18, where wave induced flow is v= (u, v, w), and the mean flow is V= (U, V, W):

$$\begin{cases} \frac{\partial \mathrm{u}}{\partial \mathrm{t}} + U\frac{\partial u}{\partial \mathrm{x}} + V\frac{\partial u}{\partial y} + W\frac{\partial u}{\partial \mathrm{z}} + u\frac{\partial U}{\partial x} + v\frac{\partial U}{\partial y} + w\frac{\partial U}{\partial z} - fv = -\frac{\partial p}{\partial x} \\ \frac{\partial \mathrm{v}}{\partial \mathrm{t}} + U\frac{\partial v}{\partial \mathrm{x}} + V\frac{\partial v}{\partial y} + W\frac{\partial v}{\partial \mathrm{z}} + u\frac{\partial V}{\partial x} + v\frac{\partial V}{\partial y} + w\frac{\partial V}{\partial z} + fu = -\frac{\partial p}{\partial y} \\ \frac{\partial \mathrm{w}}{\partial \mathrm{t}} + w\frac{\partial U}{\partial x} + w\frac{\partial V}{\partial y} + w\frac{\partial W}{\partial z} = -\frac{\partial p}{\partial z} - b \\ \frac{\partial \mathrm{u}}{\partial \mathrm{x}} + \frac{\partial \mathrm{v}}{\partial y} + \frac{\partial \mathrm{w}}{\partial \mathrm{z}} = 0 \\ \frac{\partial \mathrm{b}}{\partial \mathrm{t}} + b\frac{\partial U}{\partial x} + b\frac{\partial V}{\partial y} + b\frac{\partial W}{\partial z} + u\frac{\partial B}{\partial x} + v\frac{\partial B}{\partial y} - N^2 w = 0 \end{cases} \qquad (2-20)$$

To solve Equ.2-20, Kunze (1985) first uses the thermal-wind relation:

$$\begin{cases} -\mathrm{f}\frac{\partial \mathrm{V}}{\partial \mathrm{z}} = \frac{\partial B}{\partial x} \\ \mathrm{f}\frac{\partial \mathrm{U}}{\partial \mathrm{z}} = \frac{\partial B}{\partial y} \end{cases} \qquad (2-21)$$

Substituting Equation (2-21) into the last equation of (2-20) yields:

$$\frac{\partial \mathrm{b}}{\partial \mathrm{t}} + (\mathrm{V}\cdot\nabla)b + fu\frac{\partial V}{\partial z} + v\frac{\partial U}{\partial z} - N^2 w = 0 \qquad (2-22)$$

Next it is assumed that u, v, w, p, b satisfy the plane wave relationship:

$$\begin{cases} u = u_0 exp[i(k_x x + k_y y + k_z z - \omega t)] \\ v = v_0 exp[i(k_x x + k_y y + k_z z - \omega t)] \\ w = w_0 exp[i(k_x x + k_y y + k_z z - \omega t)] \\ p = p_0 exp[i(k_x x + k_y y + k_z z - \omega t)] \\ b = b_0 exp[i(k_x x + k_y y + k_z z - \omega t)] \end{cases} \qquad (2-23)$$

Substitute Equation (2-23) into Equation (2-20), Kunze gets:

$$\begin{cases} \left(-i\omega_0 + \dfrac{\partial U}{\partial x}\right) u_0 + \left(-f + \dfrac{\partial U}{\partial y}\right) v_0 + \dfrac{\partial U}{\partial z} w_0 + ik_x p_0 = 0 \\ \left(f + \dfrac{\partial V}{\partial x}\right) u_0 + \left(-i\omega_0 + \dfrac{\partial V}{\partial y}\right) v_0 + \dfrac{\partial V}{\partial z} w_0 + ik_y p_0 = 0 \\ -i\omega_0 w_0 + ik_z p_0 + b_0 = 0 \\ ik_x\, u_0 + ik_y\, v_0 + ik_z\, w_0 = 0 \\ -f \dfrac{\partial V}{\partial z} u_0 + f \dfrac{\partial U}{\partial z} v_0 - N^2 w_0 - i\omega_0 b = 0 \end{cases} \qquad (2-24)$$

in which $\omega_0 = \omega - \mathrm{k} \cdot \mathrm{V} = \omega - k_x u - k_y v - k_z w$;

To have a non-zero solution, we must have the determinant of the equations to be zero, i.e.:

$$\begin{vmatrix} \left(-i\omega_0 + \dfrac{\partial U}{\partial x}\right) & \left(-f + \dfrac{\partial U}{\partial y}\right) & \dfrac{\partial U}{\partial z} & ik_x & 0 \\ \left(f + \dfrac{\partial V}{\partial x}\right) & \left(-i\omega_0 + \dfrac{\partial V}{\partial y}\right) & \dfrac{\partial V}{\partial z} & ik_y & 0 \\ 0 & 0 & -i\omega_0 & ik_z & 1 \\ ik_x & ik_y & ik_z & 0 & 0 \\ -f \dfrac{\partial V}{\partial z} & f \dfrac{\partial U}{\partial z} & -N^2 & 0 & -i\omega_0 \end{vmatrix} = 0 \qquad (2-25)$$

Expanding the determinant (2-25), Kunze obtains the equation for ω_0:

$$i\left(k_x^2 + k_y^2 + k_z^2\right)\omega_0^3 + \left[-\frac{\partial V}{\partial y}k_x^2 - \frac{\partial U}{\partial x}k_y^2 - \left(\frac{\partial U}{\partial x} + \frac{\partial V}{\partial y}\right)k_z^2 + \left(\frac{\partial V}{\partial x} + \frac{\partial U}{\partial y}\right)k_x k_y + \left(\frac{\partial U}{\partial z}k_x + \frac{\partial V}{\partial z}k_y\right)k_z\right]\omega_0^2 -$$

$$i\left\{N^2\left(k_x^2 + k_y^2\right) + \left[f^2 + f\left(\frac{\partial V}{\partial x} - \frac{\partial U}{\partial y}\right) - \frac{\partial U}{\partial x}\frac{\partial V}{\partial y}\right]k_z^2 + \left(2f + \frac{\partial V}{\partial x}\right)\frac{\partial U}{\partial z}k_y k_z + \left(-2f + \frac{\partial U}{\partial y}\right)\frac{\partial V}{\partial z}k_x k_z -\right.$$

$$\left.\frac{\partial U}{\partial x}\frac{\partial V}{\partial z}k_y k_z - \frac{\partial V}{\partial y}\frac{\partial U}{\partial z}k_x k_z\right\}\omega_0 \quad + \left\{N^2\left[\frac{\partial V}{\partial y}k_x^2 + \frac{\partial U}{\partial x}k_y^2 - \left(\frac{\partial U}{\partial y} + \frac{\partial V}{\partial x}\right)k_x k_y\right] + f\left(\frac{\partial V}{\partial z}k_x - \frac{\partial U}{\partial z}k_y\right)\left(\frac{\partial U}{\partial z}k_x +\right.\right.$$

$$\left.\left.\frac{\partial V}{\partial y}k_y\right) - fk_z\left[\left(f + \frac{\partial V}{\partial x}\right)\frac{\partial U}{\partial z}k_x + \left(f - \frac{\partial U}{\partial y}\right)\frac{\partial V}{\partial z}k_y\right] - \frac{\partial V}{\partial y}\frac{\partial V}{\partial z}k_x + \frac{\partial U}{\partial x}\frac{\partial U}{\partial z}k_y\right\} = 0 \qquad (2-26)$$

Equ.2-26 is a third order polynomial equation of ω_0.

For barotropic motion, the items with vertical shear vanish. If the vertical velocity *w* is 0, then the divergence of the mean flow ($\frac{\partial U}{\partial x} + \frac{\partial V}{\partial y}$=0). $(k_x, k_y << k_z)$

With these assumptions, Kunze (1985) gets:

$$i\left(k_x^2+k_y^2+k_z^2\right)\omega_0^3 - i\left\{N^2\left(k_x^2+k_y^2\right)+\left[f^2+f\left(\frac{\partial V}{\partial x}-\frac{\partial U}{\partial y}\right)-\frac{\partial U}{\partial x}\frac{\partial V}{\partial y}\right]k_z^2\right\}\omega_0$$
$$+N^2\left[\frac{\partial V}{\partial y}k_x^2+\frac{\partial U}{\partial x}k_y^2-\left(\frac{\partial U}{\partial y}+\frac{\partial V}{\partial x}\right)k_xk_y\right]$$
$$=0 \qquad (2-27)$$

Solving Equ.2-27, it leads to:

$$\omega_0=\left[f^2+f\left(\frac{\partial V}{\partial x}-\frac{\partial U}{\partial y}\right)-\frac{\partial U}{\partial x}\frac{\partial V}{\partial y}\right]^{1/2}+\frac{\mathrm{N}^2(\mathrm{k}_\mathrm{x}^2+\mathrm{k}_\mathrm{y}^2)}{2\mathrm{f}\mathrm{k}_\mathrm{z}^2}$$
$$+\frac{\mathrm{iN}^2}{2\mathrm{f}^2\mathrm{k}_\mathrm{z}^2}\left[\frac{\partial \mathrm{U}}{\partial \mathrm{x}}\mathrm{k}_\mathrm{y}^2-\left(\frac{\partial \mathrm{U}}{\partial \mathrm{y}}+\frac{\partial \mathrm{V}}{\partial \mathrm{x}}\right)\mathrm{k}_\mathrm{x}\mathrm{k}_\mathrm{y}+\frac{\partial \mathrm{V}}{\partial \mathrm{y}}\mathrm{k}_\mathrm{x}^2\right] \qquad (2-28)$$

$\left[f^2+f\left(\frac{\partial V}{\partial x}-\frac{\partial U}{\partial y}\right)-\frac{\partial U}{\partial x}\frac{\partial V}{\partial y}\right]^{1/2}$ is usually referred as $\mathrm{f_{eff}}$. If the Rossby number $\frac{U}{Lf}$ is small or $\frac{U}{Lf}=\varepsilon$ ($\varepsilon \ll 1$), then f_{eff} can be written as $f*[1+\zeta/f]^{1/2}$, where $\zeta=\frac{\partial V}{\partial x}-\frac{\partial U}{\partial y}$ is the vorticity of the mean flow. In general, for large scale motions, $\zeta<0.2f$ (Kunze, 1985), so we can rewrite $f_{eff}\approx f*(1+\frac{1}{2}\zeta/f)=f+\zeta/2$.

Equ.2-28 can then be written as:

$$\omega_0=f+\zeta/2+\frac{N^2(k_x^2+k_y^2)}{2fk_z^2}+\frac{iN^2}{2f^2k_z^2}\left[\frac{\partial U}{\partial x}k_y^2-\left(\frac{\partial U}{\partial y}+\frac{\partial V}{\partial x}\right)k_xk_y+\frac{\partial V}{\partial y}k_x^2\right] \qquad (2-29)$$

The real part of ω_0 is $f+\zeta/2+\frac{N^2(k_x^2+k_y^2)}{2fk_z^2}$.

From Equ.2-19 which does not consider mean flow and mean flow shear: $\omega^2=f^2\frac{{k_z}^2}{{k_x}^2+{k_y}^2+{k_z}^2}+N^2\frac{{k_x}^2+{k_y}^2}{{k_x}^2+{k_y}^2+{k_z}^2}$, we can get:

$$\omega=f\frac{k_z}{\left({k_x}^2+{k_y}^2+{k_z}^2\right)^{\frac{1}{2}}}\left(1+N^2\frac{{k_x}^2+{k_y}^2}{f^2k_z^2}\right)^{1/2} \qquad (2-30)$$

If $\mathrm{k_z}>>(\mathrm{k_x}, \mathrm{k_y})$ and $N^2\frac{{k_x}^2+{k_y}^2}{f^2k_z^2}<<1$, then

$$\omega=f\frac{k_z}{k_z}\left(1+N^2\frac{{k_x}^2+{k_y}^2}{2f^2k_z^2}\right)=f+\frac{N^2(k_x^2+k_y^2)}{2fk_z^2} \qquad (2-31)$$

Comparing Equ.2-29 and Equ.2-31, their real parts are quite similar. The difference is that because of the vorticity of the geostrophic mean flow, the lower bound of internal wave band has shifted to $f+\zeta/2$ and the frequency of inertial oscillation becomes $f+\zeta/2$.

An alternative approach determining the inertial frequency with the mean flow shear was suggested by Chavane et al. (2012). They just considered the mean flow itself and the inertial force in a horizontal plane, without considering the mean flow shear and the pressure gradient. The derivation is as following:

$$\begin{cases} \dfrac{\partial u}{\partial t}+u\dfrac{\partial U}{\partial x}+v\dfrac{\partial U}{\partial y}-fv=0 \\ \dfrac{\partial v}{\partial t}+u\dfrac{\partial V}{\partial x}+v\dfrac{\partial V}{\partial y}+fu=0 \end{cases} \qquad (2-32)$$

If we define the vorticity as $\zeta=\frac{\partial \overline{v}}{\partial \mathrm{x}}-\frac{\partial \overline{u}}{\partial \mathrm{y}}$, divergence as $\delta=\frac{\partial \overline{u}}{\partial \mathrm{x}}+\frac{\partial \overline{v}}{\partial \mathrm{y}}$, shear strain as $\sigma_s=\frac{\partial \overline{v}}{\partial \mathrm{x}}+\frac{\partial \overline{u}}{\partial \mathrm{y}}$, normal strain rate as $\sigma_n=\frac{\partial \overline{u}}{\partial \mathrm{x}}-\frac{\partial \overline{v}}{\partial \mathrm{y}}$, we can rewrite the Equation (2-32) as:

$$\begin{cases} \dfrac{\partial \mathrm{u}}{\partial \mathrm{t}}+\left(\dfrac{\delta+\sigma_n}{2}\right)u+\left[\dfrac{\sigma_s}{2}-\left(f+\dfrac{\xi}{2}\right)\right]v=0 \\ \dfrac{\partial \mathrm{v}}{\partial \mathrm{t}}+\left[\dfrac{\sigma_s}{2}+\left(f+\dfrac{\xi}{2}\right)\right]u+\left(\dfrac{\delta-\sigma_n}{2}\right)v=0 \end{cases} \qquad (2-33)$$

Consider an oscillatory solution in a form of:

$$\begin{cases} u=u_0e^{i\omega t} \\ v=v_0e^{i\omega t} \end{cases} \qquad (2-34)$$

The frequency ω will have to satisfy:

$$\omega=i\frac{\delta}{2}\pm\sqrt{(f+\frac{\zeta}{2})^2-\frac{\sigma_n^2+\sigma_s^2}{4}} \qquad (2-35)$$

For the real part, if the strain rate is small, then the oscillation frequency will be $f+\frac{\zeta}{2}$.

The imaginary part means that there is energy exchange between the mean flow and the oscillation. If the divergence of the mean flow is a positive number, the energy of near inertial oscillation will increase. If the divergence of the mean flow is a negative number, the energy of near inertial oscillation will dissipate rapidly.

2.4 Case Studies of Wind Induced Near Inertial Oscillations

2.4.1 Alford's Work

Alford et al. (2012) described the wind-generated near inertial oscillation at ocean station Papa (50^0N, 145^0W) in the northeast Pacific (Fig. 2-2). The data they used lasted for 2 years. The depth of their research was concentrated in the upper 800 meters.

They separated the upward and downward propagating components and found that the kinetic energy (KE_{in}) transferring to the bottom was 3 to 7 times of the energy transferring to the surface. They also compared the near inertial oscillation kinetic energy during winter and summer. The result showed that the near inertial oscillation kinetic energy during winter was 3 to 5 times more than that of summer. They estimated that the mean vertical group velocity of near inertial oscillation (c_{gz}) was about 0.015cm/s. They also calculated the energy flux by means of c_{gz}*KE_{in}. After comparing with the near inertial oscillation energy in the mixed layer from a surface buoy, they concluded that 12% to 33% of the energy input into the mixed layer reached down to 800 meter. To get inertial velocities from the mooring data, they applied a fourth-order Butterworth filter to the velocity $V=u+iv$ in the time domain twice: one is $1.15f$ low pass and the other is $0.9f$ high pass, where f is the Coriolis parameter. This data processing is problematic and it causes a great loss of energy.

Figure 2-2 Location of Station Papa (denoted by the yellow arrow) (From Google Maps, 2012)

Their method however is problematic. To illustrate this problem, here is an example: suppose that we have a function $Z = \sum_{i=1}^{100} \sin(2\pi it)$ (where i is an integer), Z is a summation of a series of sine functions, with frequencies from 1 to100 Hz, respectively. If we apply a Fourier Transform to Z in the time domain (from 1s to 1000s), we can get Fig. 2-3a, while all the energy of each frequency (1 to 100 Hz) is 1. If we intend to focus on the f=50 Hz signal, as done in Alford (2012), we apply a band pass filter of $\{0.9, 1.15\}f$ to Z. The result is shown in Fig. 2-3b. In Fig. 2-3b, the cyan line demonstrates the power spectrum of Z before the bandpass filtering, the red line is after the bandpass filtering and the cyan line is the cut off frequency {0.9, 1.15}*50Hz.

We can see that the bandpass filtering cut half of the energy within the bandpass range. In addition, the frequency beyond the bandpass range still has some energy. A proper application of the bandpass filtering is thus needed.

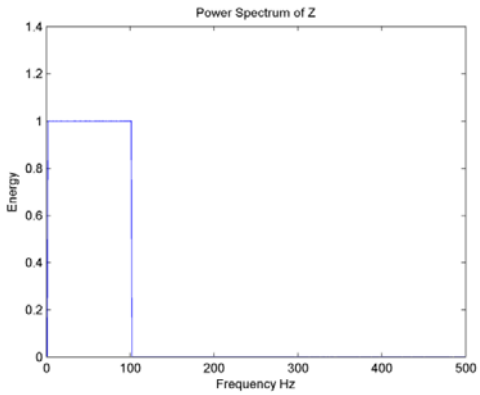

Figure 2-3a Power Spectrum of Z

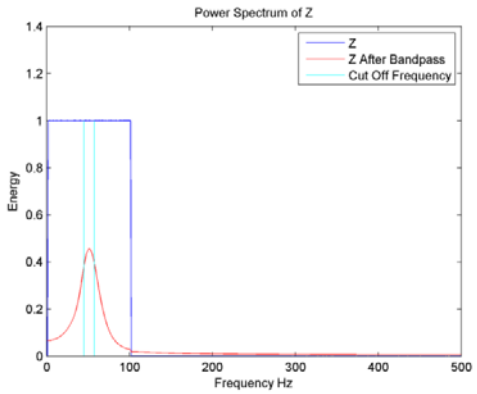

Figure 2-3b Comparing the Power Spectrum of Z Before and after the bandpass

2.4.2 Shay and Elsberry's Work

In September 1979, Hurricane Frederic passed the U.S. Naval Oceanographic Office current meter arrays and an Ocean Thermal Energy Conversion mooring in the Gulf of Mexico. Shay and Elsberry (1987) observed near inertial oscillations at all depth of the data. In their work, the frequencies of near inertial oscillations were 1% to 6% blue-shifted. Within hours of the hurricane passage, the vertical wave length responded at 1000m depth. The vertical group velocity c_{gz} for the first baroclinic mode was 0.15cm/s within 2

inertial periods after Frederic passed and for the second baroclinic mode, c_{gz} is 0.03cm/s within 7 inertial periods which is quite similar to the c_{gz} in Alford's case.

They also concluded that the sloping bottom effect of the study area contributed an extra 5% to 6% variance in addition to the mean flow shear.

2.4.3 Sun et al.'s Work

In 2004, Typhoon Chanchu passed a mooring site of an acoustic Doppler current profiler (ADCP) in the western South China Sea and excited large near inertial oscillations. Sun et al. (2011) observed a 4% blueshift of the near inertial oscillation frequency right after the passage of the typhoon. After calculating the vorticity of the mesoscale eddies with satellite data, they concluded that the blueshift is partially due to the mean flow shear which is consistent with the assumption of Kunze (1985) and Chavane (2012).

In their research, the latitude of the mooring is around 14^0N, where the near inertial frequency is half of the diurnal tide frequency, which implies that parametric subharmonic instability (PSI) will cause energy exchange between the diurnal and the near inertial oscillation. The PSI effect is an effect that can transfer energy from higher frequency F1 to lower frequency F2 as far as F1 is twice of F2 (Alford, 2008; Young et al., 2008). PSI effect should be taken into account when we study inertial oscillations in critical latitudes where local inertial frequency is half of the diurnal tides or semi-diurnal tides (Sun et al., 2011).

2.5 Motivation and Objectives

As discussed above, the wind generated near inertial oscillations has been extensively discussed, though not all of it has been well understood. As proposed by Kunze (1985), the lower bound of internal wave band, or the inertial frequency should shift from the local Coriolis frequency f to $f + \zeta/2$ under the effect of local quasi-geostrophic shear. This theory has been widely applied to explain the observations (e.g., Elipot et al., 2010; Shay, 1998; Sun et al., 2011; Van Meurs, 1997; Zhai et al., 2005), while most of them only achieved ambiguous correlations between the theoretically results and the true ones from the power spectrum. Also, the examinations are mostly constrained within a short time event. There has been no work to verify the theory.

The CSI mooring observations in 2005 provide us with the rare opportunity to examine the above theory. Furthermore, the deep ocean mooring makes the study of near inertial oscillations of different depth to the passage of high intensity hurricanes possible. We can also take advantage of the high resolution ADCP measurements to discuss the phase variations of near inertial oscillations in the surface layer and bottom layer. These motivate us to do this study.

As a result, in this study, we mainly focus on: 1) Variations of frequencies of near inertial oscillations 2) Transferring of near inertial oscillations energy from surface water to the deep ocean. 3) Phase variations of near inertial oscillations at different depths in central Gulf of Mexico. The Loop Current in this area also plays an important role in the recorded currents (Welsh et al., 2009; Oey and Wang, 2009).

2.6 Study Area

Our study area is in the central Gulf of Mexico, around 25.5^{o}N, 87^{o}W (the deep ocean mooring, Welsh et al., 2009). The water depth is around 3356m. The water column can be divided into 2 major layers with respect to the dynamics (Welsh et al., 2009). The upper layer, ranging from the surface to 750m, is dominated by the Loop Current and Loop Current rings. The lower layer is from 1000m to the sea bottom where it is generally barotropic. Between 750 and 1000m is the transition zone of these two layers. It appears that when the Loop Current propagates to the north, the upper layer and the lower layer will show some consistency. However, decoupling of the two layers happens frequently (Welsh et al., 2009). The stratification can also be seen from Conductivity, Temperature, Depth (CTD) sensor data. The CTD data is from a research vessel at the beginning of the 4th deployment of a research program funded by the Bureau of Ocean Energy Management, Regulation and Enforcement (BOEMRE) (BOEMRE Contract: 1435-01-04-CA-32806-36189 (M05AZ10669)). The salinity and temperature profile from the cruise data are shown in Fig. 2-4. It is apparent that the lower layer appears to be barotropic from Fig.2-4. Temperature in the lower layer is generally constant. Salinity increases slightly from 1000m depth to 1500m depth and then keeps almost constant from 1500m to the bottom. The possible answer to this is that in addition to the sinking of the salty

and cold flow from the deep Caribbean Basin over the Yucatan Channel, some hyper-saline basins and/or salt domes may exist on the bottom of GoM. The lower layer thus presents a rather homogeneous state which implies mixing. Deep eddies are supposed to be one of the main factors in mixing (Welsh et al., 2009). For the upper layer, temperature decreases at an almost constant rate with depth; salinity reaches the maximum at a depth around 200m and minimum at a depth around 900m. The maximum salinity is corresponding to the Subtropical Underwater which is the salty water produced by the excess evaporation in the western tropical Atlantic Ocean. The minimum is corresponding to the Sub-Antarctic Intermediate Water (Welsh et al., 2009).

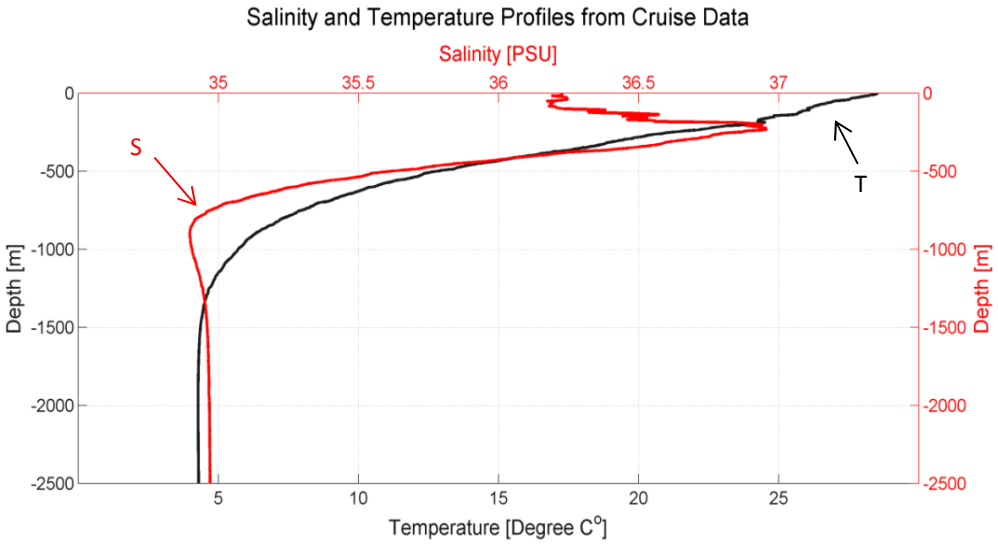

Figure 2-4 Temperature and Salinity Profile at the Mooring Station (Red line denotes salinity and black line denotes temperature) obtained on a research vessel at the beginning of 4th deployment of a research program funded by BOEMRE

2.7 The Mooring Station

The mooring station is at 25.5^0N, 87^0W (Fig. 2-5). The reason why the mooring was deployed here is that this location is a sensitive point for the shedding process of the Loop Current (Welsh, 2009). This mooring project with 5 deployments was funded by BOEMRE. The data we used is from the 4th deployment. This deployment extends from May. 29th, 2005 to Jun. 15th, 2006.

2.8 2005 Hurricanes

From Jun. 2005 to Oct. 2005, there were 6 hurricanes and tropical storms passed within a 350 km radius around the mooring (Fig.2-5, Tab. 2-1). Four of them are major hurricanes (higher than Category 3). Among them Hurricane Katrina and Rita are the strongest and closest to the mooring.

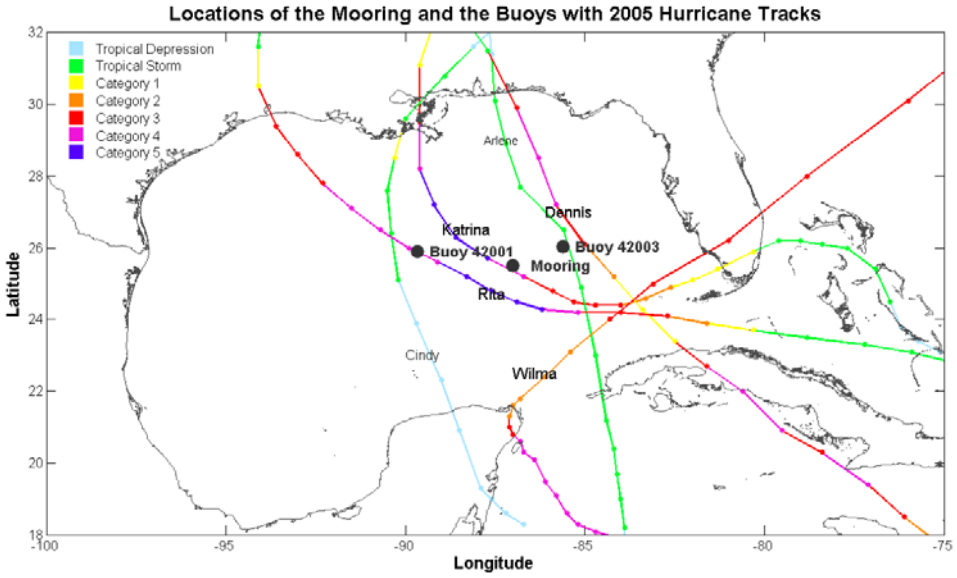

Figure 2-5 Locations of the Mooring and the Buoys with 2005 Hurricane Tracks

Table 2-1 Hurricanes Passing the Mooring Site

Hurricane Name	Time	MSW (kts)	Distance (km)
Arlene	6-11 00:00	59	180
Cindy	7-5 6:00	34	330
Dennis	7-10 0:00	110	205
Katrina	8-28 12:00	144	15
Rita	9-22 6:00	154	95
Wilma	10-23 18:00	89	300

*The data is from National Hurricane Center
*MSW: It is short for Maximum Sustained Wind
*Time: When the center of the Hurricane is the closest to the mooring, the temporal resolution of this track data is 6 hours.
* Distance: the distance is roughly estimated based on the 6-hour resolution track data, the accuracy of the distance is around 5km.

3. Data Description and Methodology

This chapter describes the data we used for analysis and methodology of the analysis. The data are from the CSI mooring, 2 National Buoys and Colorado Center for Astrodynamics Research (CCAR). The analysis consists of vertical interpolation, temporal interpolation, high-pass filter and rotary spectra analysis.

3.1 Data Description

3.1.1 Mooring Data

The mooring has 2 Acoustic Doppler Current Profilers (ADCP), 13 Anderaa current meters and 11 CTDs. One ADCP was set as up-looking at 140 meters below the surface; the other one was set as down-looking at 3200m. The 1st bin was 10.34 meter away from the transducer and the bin size was 8 meters. The sampling time interval for the ADCPs was a large 4.5 hours, due to an incorrect setting; however it returned good data for the most part. The 13 current meters were at 250, 350, 450, 600, 750, 875, 1000, 1200, 1500, 2000, 2500, 3000, 3186 meters below the surface, respectively. The data we used in this research is indicated in Table 3-1, while the structure of the mooring is in Fig. 3-1. The sampling time interval for the current meter was 1 hour. The 11 Microcats were at 145, 351, 749, 1000, 1501, 1800, 2001, 2500, 3001, 3187, 3297 meters below the surface (Welsh, 2009), respectively. The sampling time interval for the Microcats is 0.5 hour.

Since our objective is to examine the variations of NIOs during the 2005 hurricane season, we only use the ADCP and current meter data from June 1st to November 10th, 2005. The structure of the mooring is shown in Fig.3-1.

Table 3-1 Data Used in This Research

Instrument Name	Design Depth [m]	Start Date	End Date
ADCP	140	6-1-2005	11-10-2005
CURRENT METER	250	6-1-2005	11-10-2005
CURRENT METER	350	6-1-2005	11-10-2005
CURRENT METER	450	6-1-2005	11-10-2005

Table 3-1 Continued

Instrument Name	Design Depth [m]	Start Date	End Date
CURRENT METER	600	6-1-2005	11-10-2005
CURRENT METER	750	6-1-2005	11-10-2005
CURRENT METER	875	6-1-2005	11-10-2005
CURRENT METER	1001	6-1-2005	11-10-2005
CURRENT METER	1500	6-1-2005	11-10-2005
CURRENT METER	1200	6-1-2005	11-10-2005
CURRENT METER	2000	6-1-2005	11-10-2005
CURRENT METER	2500	6-1-2005	11-10-2005
CURRENT METER	3000	6-1-2005	11-10-2005
CURRENT METER	3186	6-1-2005	11-10-2005
ADCP	3190	6-1-2005	11-10-2005

3.1.2 Buoy Data

In this study, we also used buoy data from the National Data Buoy Center (NDBC), which includes wind direction, wind speed, wind gust, wave height, dominant wave period, average wave period, mean wave direction, atmospheric pressure, pressure tendency, and air and water temperatures. The sampling time interval is 1hour.

We choose the data from Buoy 42001 and Buoy 42003 (Fig. 2-6). They were the closet buoys to the mooring. Buoy 42001 (LLNR 1400) was located in the central gulf (25.888^{o}N, 89.658^{o}W). Buoy 42003 (LLNR 1395) was located in the east gulf (26.044^{o}N 85.612^{o}W). Air temperature was measured at 4 meters above mean sea level; anemometers at 5 meters above mean sea level; and sea surface temperature at 1 meter below sea surface. The water depth at Buoy 42001 was 3365 meters and the depth at Buoy 42003 was 3282.7 meters (NDBC website, 2012). The data from Buoy 42001 covers the whole time period (Jun. 1st, 2005 to Nov. 10th, 2005), except after Nov. 1st when the wind direction data is missing. Buoy 42003 did not record data from Aug. 28th, 4:50 to October 6th 22:00. As a result, much of the wind information during Hurricanes Katrina and Rita is missing in the data from Buoy 42003.

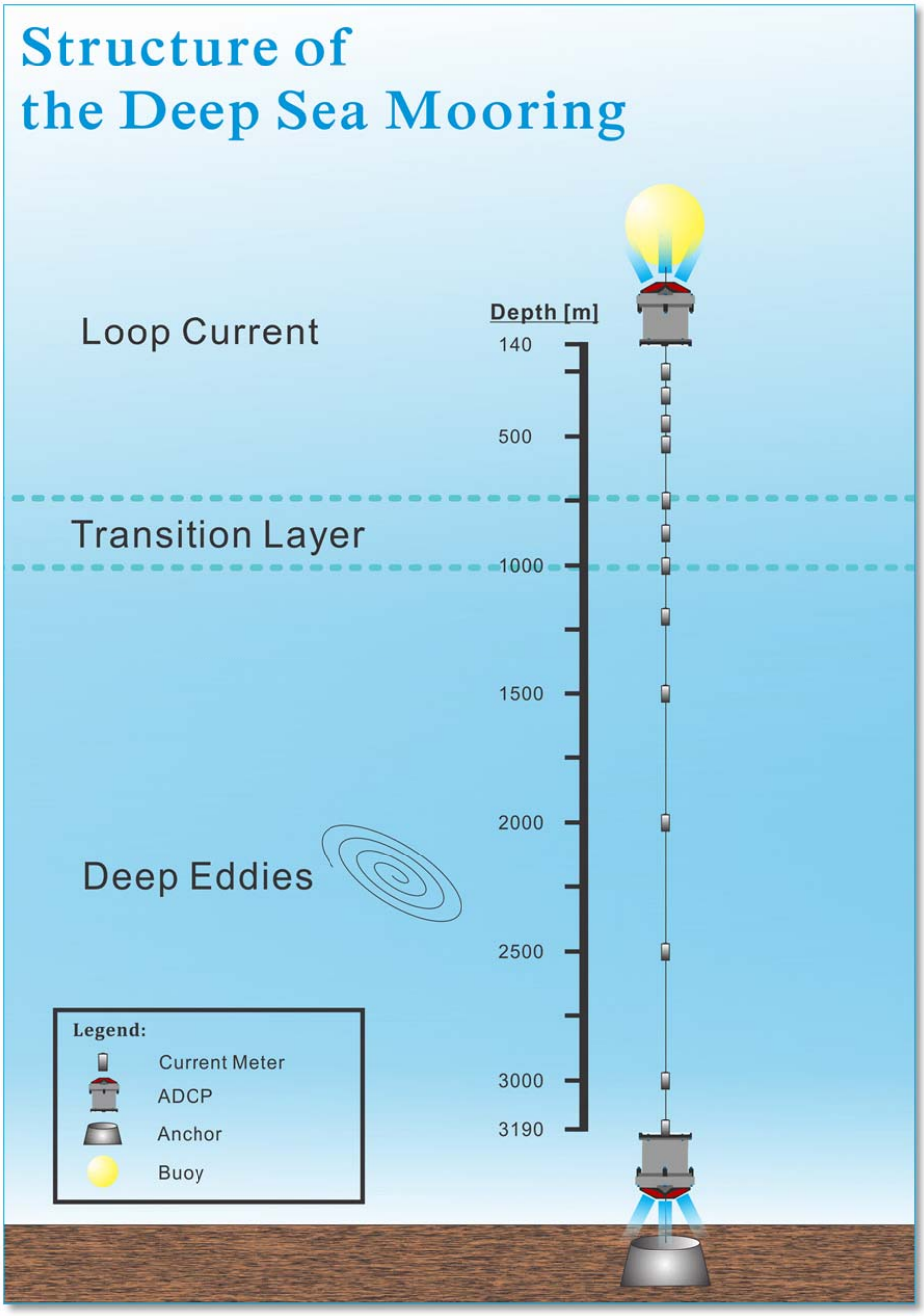

Figure 3-1 Structure of the Deep Sea Mooring (Only the instruments of which data was used is plotted in this figure, not to scale)

3.1.3 Sea Surface Height (SSH) Data

We acquired the SSH data from the Colorado Center for Astrodynamics Research (CCAR). The SSH data from satellite covers less than 5km width along the track. The satellite data can only scan the same point after more than one month period of time. Fig.3-2 (a) and Fig. 3-2 (b) show the tracks of multiple SSH satellites within 1 month and from a single satellite within 18 days (Robert, 2013). The final SSH data is a time interpolation product from multiple satellite data along the narrow tracks within more than 1 month. This will cause time lags between the real velocity field and the one calculated from SSH data. The daily data is generally based on the Operational Geophysical Data Records (OGDR) for Satellite Jason-1, Ocean Surface Topography Mission (OSTM) for Satellite Jason-2 and the Fast-delivery Geophysical Data Records (FGDR) for Satellite Envisat. Operational Geophysical Data Records (OGDR) is a near real-time operational product delivered to users within 3 - 5 hours after data collection. Ocean Surface Topography Mission (OSTM) is an international satellite mission to get continuous sea surface height data. Fast-delivery Geophysical Data Records (FGDR) is also a program providing near-real-time sea surface height anomaly data. All the data was distributed by the Physical Oceanography Distributed Archive Center at the NASA Jet Propulsion Laboratory, Pasedena, CA. The spatial resolution of the daily SSH data is 0.25^{o} (Fig. 3-3). It covers the study area.

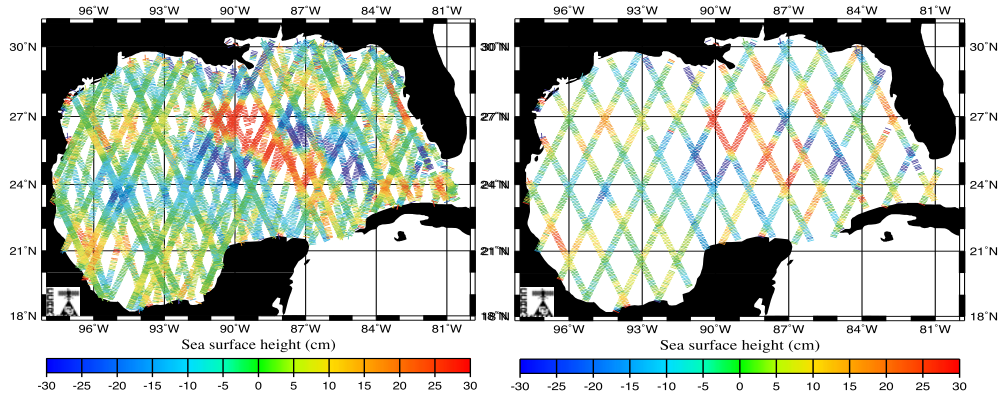

(a) (b)

Figure 3-2 (a) Satellite Tracks from Multiple Satellites from Mar.1st 2001 to Apr. 1st 2001. (b) Satellite Track from a Single Satellite from Mar. 3rd 2001 to Mar. 21st 2001. (From Robert, 2013)

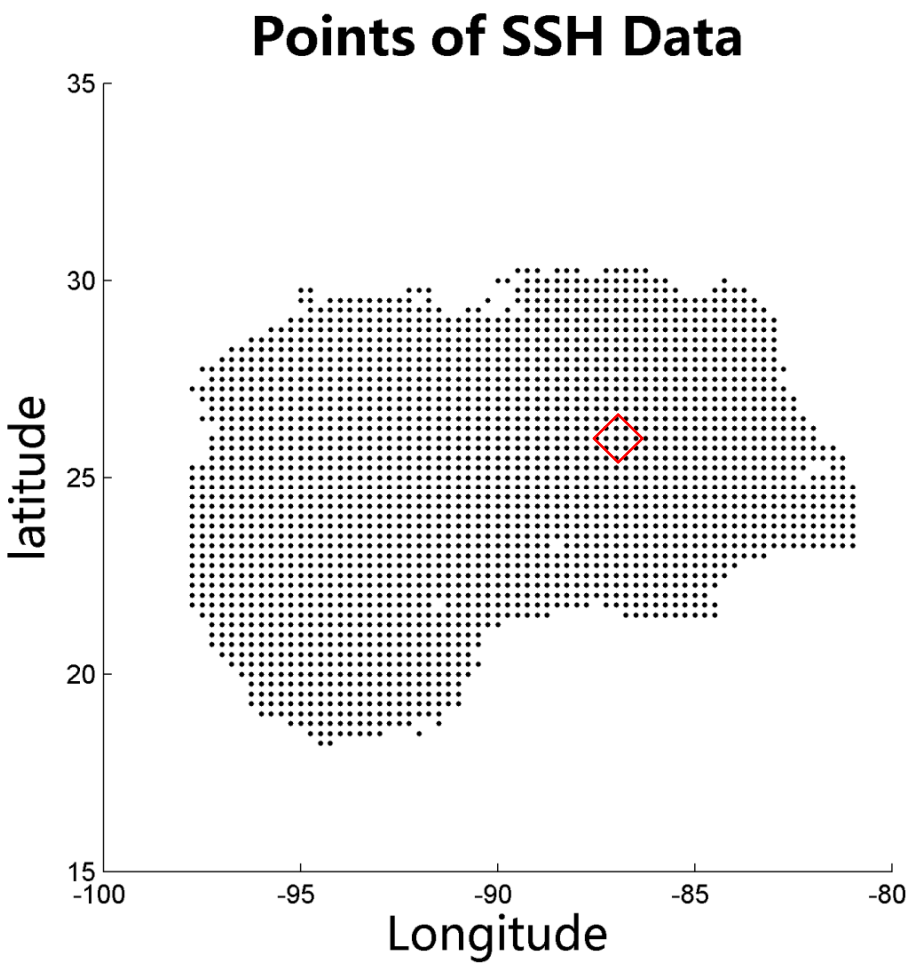

Figure 3-3 Points of SSH Data in the Gulf of Mexico (The red diamond indicates the SSH data we used)

3.1.4 Hurricane Track Data

The hurricane track data is from National Hurricane Center (NHC). The data includes date, time, latitude, longitude, maximum sustained surface wind speed, and central surface pressure. The time resolution is 6-hour. The hurricane track data was used to estimate the closest distance between hurricane center and the mooring and when they became closest. We can estimate the distance with accuracy around 5km determined by the temporal resolution of the track data.

3.2 Methodology

3.2.1 Vertical Interpolation

As demonstrated in Fig.3-1, all the instruments (including ADCPs and current meters) were tied to the mooring string. The bottom of the string was fixed by an anchor. A buoy was at the top of the string to make the mooring straight. However, when strong current occurs in the mooring area, the instruments of the mooring will not remain in their designed depths (Fig.3-4) and the entire mooring will be forced to bend with the current (Fig.3-5). After the strong current, the instruments of mooring will gradually come back to their designed depths again. This process will cause the variations of instrument depths (Meinen, 2008).

The water pressure was measured by pressure sensors. These pressure sensors are within the instruments, such as ADCPs and current meters, while they were at the same depth as the instruments. We assumed that the density of the sea water is constant and equals to 1.025g/cm^3; the gravitational acceleration is 9.8 m/s^2. With the pressure equation:

$$h = p/\rho g \qquad (3-1)$$

we get the depths of each instrument.

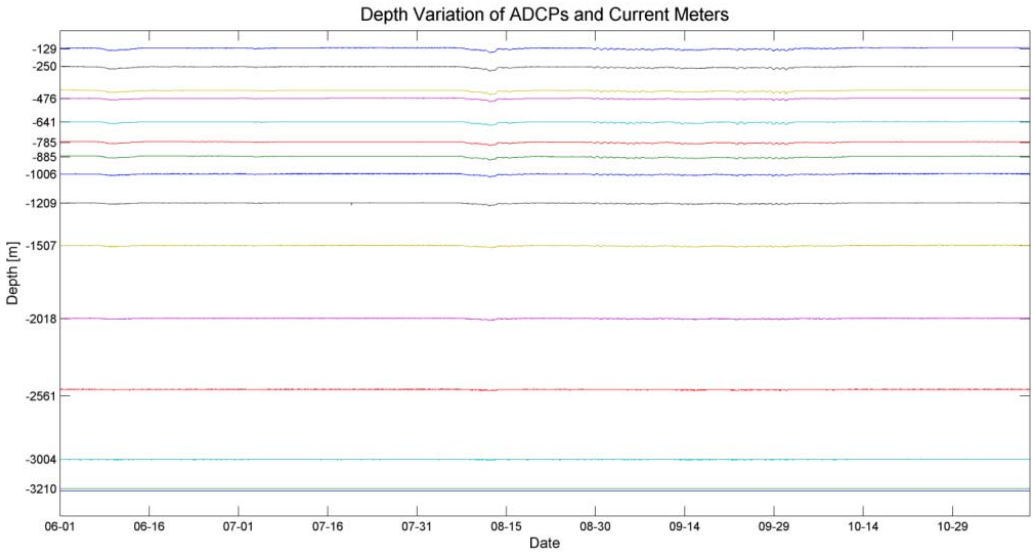

Figure 3-4 Depth Variations of ADCPs and Current Meters

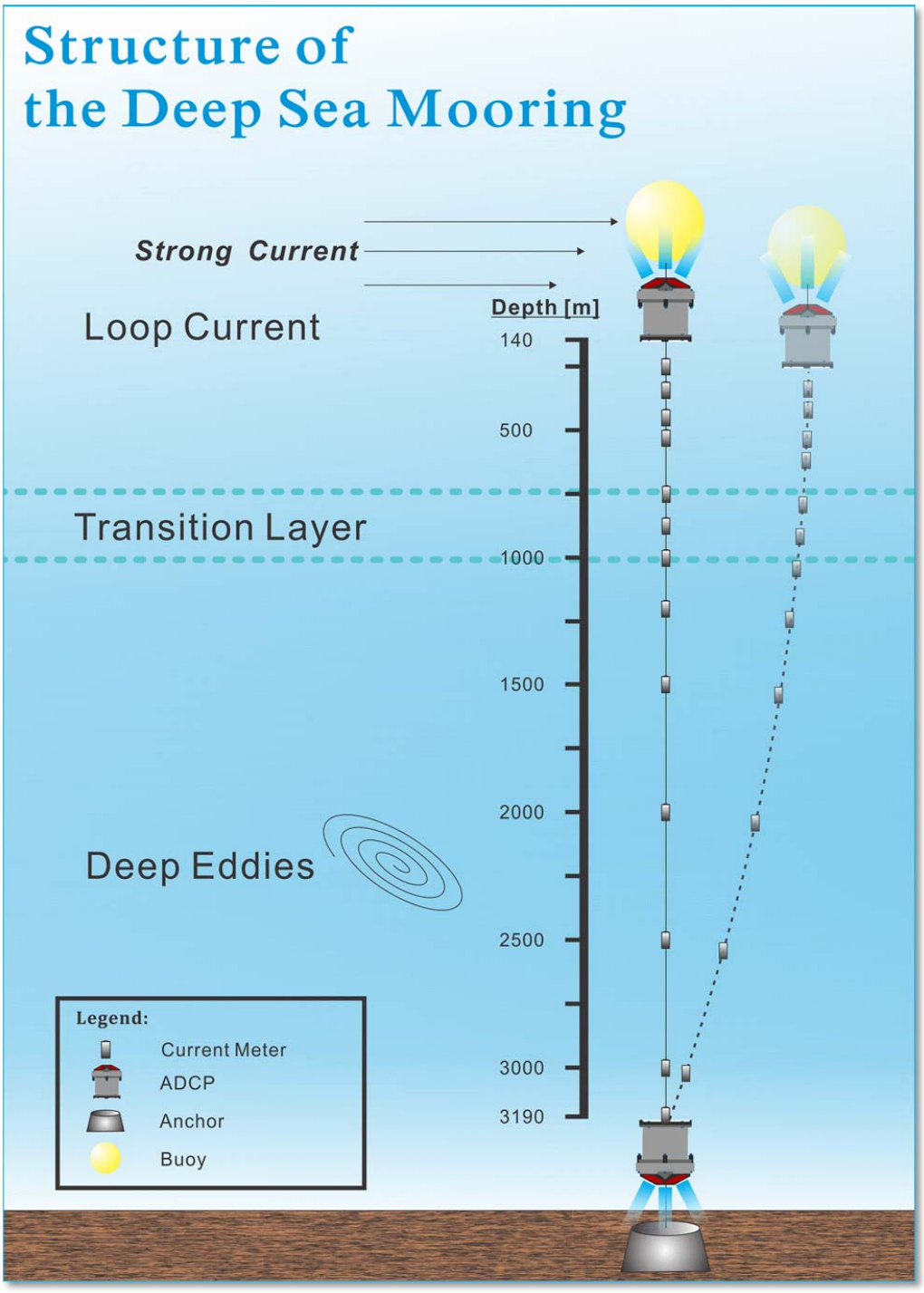

Figure 3-5 Schematic Diagram of the Mooring under the Effect of Strong Current (not to scale)

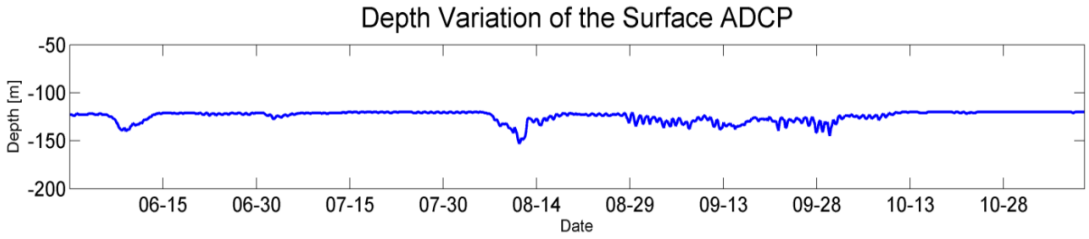

Figure 3-6 Depth Variations of the Surface ADCP

From Fig.3-4 and Fig.3-6, we find that these instruments went up and down during the study period. For convenience of processing, we need to interpolate these time series of velocities onto fixed vertical positions. If we apply linear interpolation, we need to choose the lowest depth of each layer for interpolation to avoid the problem of extrapolation which will return not-a-number (NaN) by MATLAB. However, this method is problematic if the lowest depth of the instrument, causing by extreme event, is much lower than its designed depth. For instance, most of the time, the upper most bin of the ADCP was around 49m; when a strong current occurred, the depth went down to as low as 79m. If we interpolate all the current speed of this bin to 79m, it cannot accurately represent the micro-scale environment dynamics through the vertical profile, especially when the bin size of our ADCP (8m) is just 1/4 of this depth variation. Using the Precise Cubic Hermite interpolating polynomial (PCHIP) can avoid this problem, since we can interpolate the current data to the average depth of the instrument with PCHIP. After the depth interpolations, we have the current velocity information at the depths of 3296, 3288, 3280, 3272, 3264, 3256, 3248, 3240, 3232, 3210, 3004, 2561, 2018, 1507, 1209, 1006, 885, 785, 641, 476, 422, 250, 129, 121, 113, 105, 97, 89, 81, 73, 65, 57, and 49 meters (33 layers), respectively, where the data of the highest 11 depths and lowest 9 depths are from the two ADCPs.

3.2.2 Temporal Interpolation

As described in Table 3-1, we used the data of 2 ADCPs and 13 current meters from Jun. 1st, 2005 to Nov. 10th, 2005 (163 days). Since the sampling time intervals were different (ADCP 4.5h, current meter 1h), we did interpolations to the ADCP and current meter data in time domain so that they all have a temporal resolution of 0.5h to agree with the CTD data.

3.2.3 Fast Fourier Transform (FFT)

The Fast Fourier Transform is a technique to transfer dataset from the time domain to frequency domain. We can get power spectrum (amplitudes of each frequency against frequencies) based on FFT. Comparing to the original Fourier Transform method, it uses the exponential format instead of sine, cosine format; thus largely increases the computing speed (Emery and Thompson, 2001). The frequency resolution of the power spectrum is 1/T, where T is the time length of the dataset. The longer the time we choose, the higher the resolution we can get (Fig.3-7). However, if the time period is too long, we will not be able to clearly identify events from the spectrum.

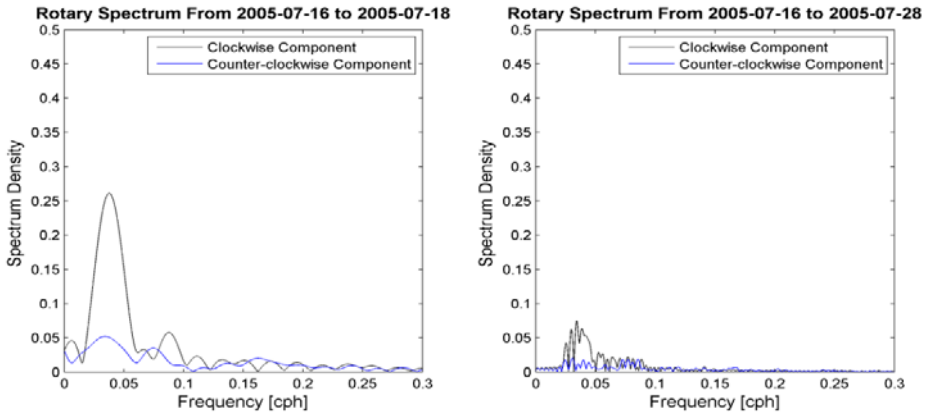

Figure 3-7 Comparison of Different Time Length with Different Frequency Resolutions

3.2.4 High Pass Filter

In this study, a 6th-order Butterworth high-pass filter with a cutoff frequency of 1/40 hour^{-1} was used to remove low frequency current. Since local inertial period is 27.8 hr, a 40 hour high-pass filter can well cut off the low frequency components and remain the near inertial oscillations.

3.2.5 De-tide

The inertial period at the mooring site is 27.8 hour, which is close to the local diurnal period. We cannot use low pass filter to separate near inertial energy and diurnal tidal energy. The way to do it is using harmonic analysis. In this study, we used the Tidal Analysis Tool Box of MIKE 21 to eliminate all the tidal components. The Tidal Analysis Tool Box of MIKE 21 can give us the tidal residuals as far as we input a long enough time series of current data and the location of the current.

3.2.6 Rotary Spectra

The near inertial oscillations in the north (south) hemisphere are clockwise (counter-clockwise). Rotary Spectra is a technique which can separate clockwise components and counter-clockwise components of the current. Imagine that the current velocity is V, of which the mean flow has been removed. We can separate V into 2 components: u and v (u is the west-east velocity component and v is the south-north component,). These 2 components can be expressed as Equ.3-1 and Equ.3-2 based on Fourier Transform theory, where t is time, f_js are frequencies and a_j, b_j, c_j, d_j, are amplitudes (O'Brien and Pillsbury, 1974):

$$u = \sum_{j=1}^{\infty} \{a_j \cos(2\pi f_j t) + b_j \sin(2\pi f_j t)\} \qquad (3-1)$$

$$v = \sum_{j=1}^{\infty} \{c_j \cos(2\pi f_j t) + d_j \sin(2\pi f_j t)\} \qquad (3-2)$$

If we express V as:

$$V = u + i*v \qquad (i=\sqrt{-1})$$

$$= \sum_{j=1}^{\infty} \left\{ (a_j + i*c_j) \frac{e^{i2\pi f_j t} + e^{-i2\pi f_j t}}{2} + (b_j + i*d_j) \frac{e^{i2\pi f_j t} - e^{-i2\pi f_j t}}{2i} \right\}$$

$$= \sum_{j=1}^{\infty} \left\{ \frac{1}{2}[a_j - b_j + i(c_j - d_j)]\, e^{i2\pi f_j t} + \frac{1}{2}[a_j + b_j + i(c_j + d_j)]\, e^{i2\pi f_j t}\, e^{-i2\pi f_j t} \right\} \qquad (3-3)$$

If $A_j=(a_j-b_j)^2+(c_j-d_j)^2$, then we can express $(a_j-b_j)/A_j$ as $\cos \alpha_j$ and $(c_j-d_j)/A_j$ as $\sin \alpha_j$.

If $B_j=(a_j+b_j)^2+(c_j+d_j)^2$,then we can express $(a_j+b_j)/B_j$ as $\cos \beta_j$ and$(c_j+d_j)/B$ as $\sin \beta_j$.

Then we can rewrite Equ.3-3 as:

$$V = \sum_{j=1}^{\infty} \left\{ \frac{1}{2} A_j (\cos\alpha_j + i\sin\alpha_j) e^{i2\pi f_j t} + \frac{1}{2} B_j (\cos\beta_j + i\sin\beta_j) e^{-i2\pi f_j t} \right\}$$

$$= \sum_{j=1}^{\infty} \left\{ \frac{1}{2} A_j e^{i\alpha_j} e^{i2\pi f_j t} + \frac{1}{2} B_j e^{i\beta_j} e^{-i2\pi f_j t} \right\}$$

$$= \sum_{j=1}^{\infty} \left\{ \frac{1}{2} A_j e^{i(2\pi f_j t + \alpha_j)} + \frac{1}{2} B_j e^{-i(2\pi f_j t - \beta_j)} \right\} \qquad (3-4)$$

Here, $A_j/2$ represents the amplitudes of counter-clockwise component of V (with positive frequency) and $B_j/2$ represents the amplitudes of clockwise component (with negative frequency). α_j and $-\beta_j$ are the initial phases of the two components.

If we apply FFT to $V = u + i * v$ time series, then the first half of the resultant matrix [w] represents $A_j s$ from low frequency to high frequency and the rest half represents $B_j s$ from high frequency to low frequency. So we need to flip the left side and right side of the second half of [w]. Then we can get the rotary spectra (Emery and Thompson, 2001).

3.2.7 Calculation of Near Inertial Energy

Since one of our objectives is to determine the variations of near inertial energy during hurricanes, we will calculate the power spectrum of the near inertial oscillations as a function of time. We will use the square of the velocity V to represent the near inertial energy at each depth. Here V is filtered by a 40 hour high pass filter, which includes components at local inertial frequency. While the low pass filtered data will have non-inertial motions also, the inertial oscillations are found to be dominant and the result we obtained is representative of the near inertial oscillations.

3.2.8 Identify Near Inertial Frequency from Rotary Spectra

One of the main objectives of this study is to discuss the variations of near inertial oscillation frequency. For some cases, we can easily do it with the rotary spectra, when there is a single high peak for clockwise components in the rotary spectra. In this situation, we can treat the frequency corresponding to this high peak as the frequency of the near inertial oscillation.

However, sometimes there are several comparable high peaks around the inertial frequency (Fig.3-8(a)).It is hard to decide which one can better represent the near inertial frequency. In this study, we will just use the highest peak as the near inertial frequency for both cases. This will be discussed in the Results and Discussion Chapter.

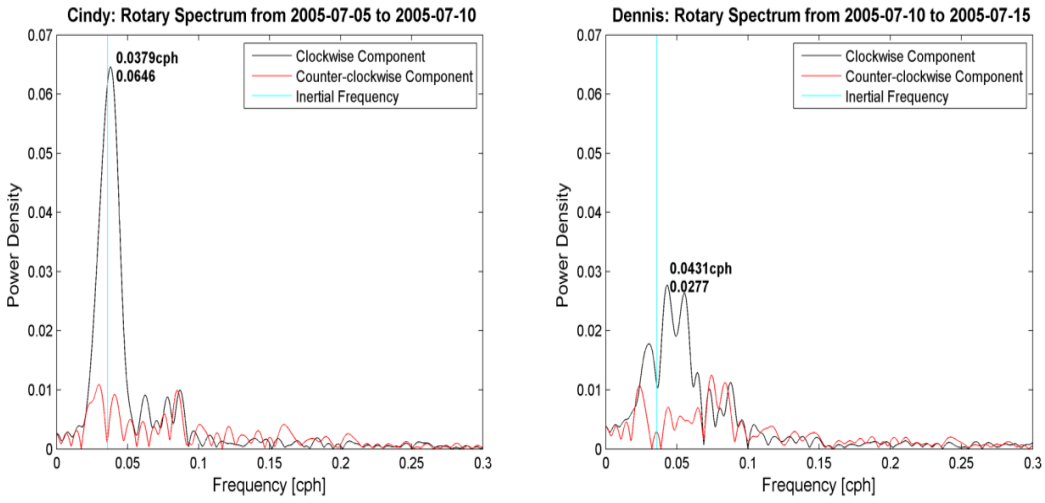

(a) (b)

Figure 3-8 Variations of Relative Heights of Peaks

3.2.9 Calculation of the Near Inertial Oscillation Frequency from SSH Data

As Kunze (1985) showed, under the influence of local vorticity, the inertial frequency will shift from local inertial frequency *f* to:

$$f = f + \zeta/2 \qquad (3 - 5)$$

where ζ is the local vorticity. We will examine this theory with the SSH data. The key is the calculation of the local vorticity. The way we calculated the vorticity is as following. Fig. 3-9 demonstrates the data points we use to calculate the vorticity at the mooring site (Point 7).

The vorticity of the mooring can be expressed as:

$$\zeta = \frac{\partial \bar{v}}{\partial x} - \frac{\partial \bar{u}}{\partial y} \qquad (3-6)$$

The velocity gradient $\frac{\partial \bar{v}}{\partial x}$ can be acquired from the difference of time averaged *v* component between Point 8 and Point 6; $\frac{\partial \bar{u}}{\partial y}$ can be calculated by the difference of time averaged *u* component between Point 3 and Point 11. The time length T of each average ($\bar{u}, \bar{v}$) is corresponding to the length of the time window in rotary spectra.

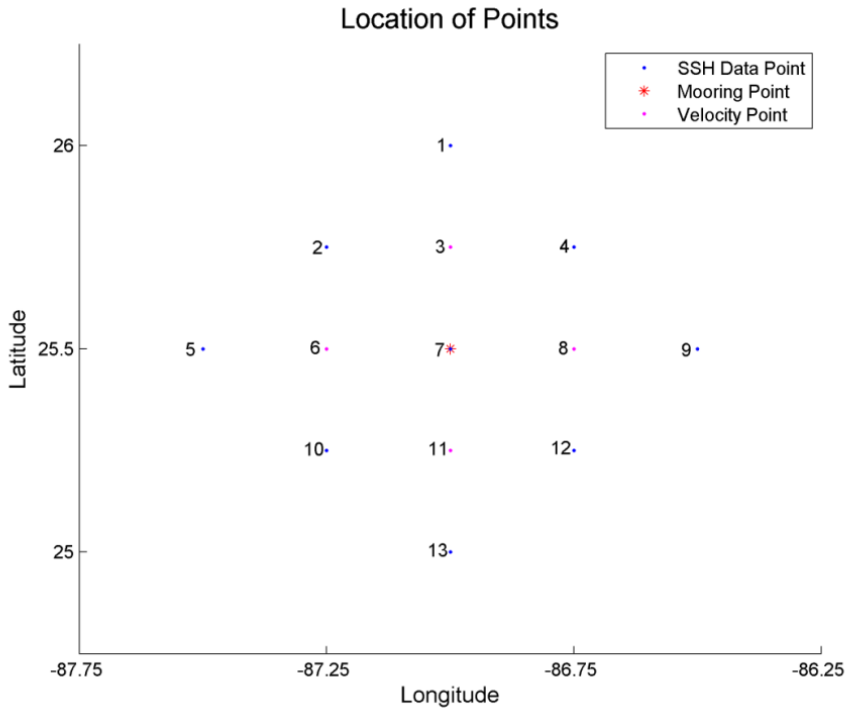

Figure 3-9 Locations of Points

So Equ.3-6 can be re-expressed as:

$$\zeta = \frac{\overline{v_8} - \overline{v_6}}{x_8 - x_6} - \frac{\overline{u_3} - \overline{u_{11}}}{y_3 - y_{11}} \qquad (3-7)$$

$x_8 - x_6 = 0.5 * 2 * \pi * \frac{R}{360} * \cos(25.5^0)$, it is the distance between Point 8 and Point 6; $y_3 - y_{11} = 0.5 * 2 * \pi * R/360$, it is the distance between Point 3 and Point 11. R=6371km is the radius of the earth (World Geodetic System, 1984). The velocity of Point 3, 6, 8, 11 can be calculated from SSH data based on the quasi-geostrophic assumption.

The balance between horizontal pressure gradient and Coriolis force will result in a geostrophic flow. It can be described by the following equation (Gill, 1982):

$$\begin{cases} fv_g = \frac{1}{\rho}\frac{\partial \rho g h}{\partial x} \\ -fu_g = \frac{1}{\rho}\frac{\partial \rho g h}{\partial y} \end{cases} \qquad (3-8)$$

The solution of geostrophic velocities is Equ.3-8, if the density of the water is a constant,

$$\begin{cases} v_g = \dfrac{g}{f}\dfrac{\partial h}{\partial x} \\ u_g = -\dfrac{g}{f}\dfrac{\partial h}{\partial y} \end{cases} \quad (3-9)$$

So for instance, the geostrophic velocity of Point 3 can be expressed as:

$$\begin{cases} v_{g3} = \dfrac{g}{f}\dfrac{h_4 - h_2}{x_4 - x_2} \\ u_{g3} = -\dfrac{g}{f}\dfrac{h_1 - h_7}{y_1 - y_7} \end{cases} \quad (3-10)$$

The quasi-geostrophic flow assumption requires a slow change of velocity. The velocities based on this assumption can be written as (Gill, 1982):

$$\begin{cases} u \approx u_g - \dfrac{1}{f}\dfrac{\partial v_g}{\partial t} \\ v \approx v_g + \dfrac{1}{f}\dfrac{\partial u_g}{\partial t} \end{cases} \quad (3-11)$$

Through this we got the 8-day averaged quasi-geostrophic velocity of Point 3, 6, 8, 11 and vorticity of the mooring (Point 7). Near inertial oscillation frequencies could also be acquired from Equ.3-5.

4. Results and Discussions

The vertical profile in this study is separated into 3 layers based on the local dynamics and the vertical distribution of the instruments. The surface layer is from 49m to 129m. The data is from the surface ADCP and provides us with information of near inertial oscillations above the thermocline (Fig. 2-5). The data of the currents at 49m depth is from the uppermost bin of the surface ADCP. The mid-layer is from 200m to 1500m, the data is from the current meters. 1500m is the deepest depth where we can find significant near inertial oscillation through baroclinic processes. The bottom layer is from 3232m to 3296m. The data is from the bottom ADCP and provides us with the barotropic response of near inertial oscillations to severe hurricanes. We did not analyze the near inertial oscillations between 1500m to 3232m. First, the water column at this depth is generally homogeneous and barotropic. Second, we did not observe significant near inertial oscillations at this depth. Third, there were only 4 current meters to cover 1500m water column, we cannot capture the details with this low spatial resolution.

4.1 Surface Near Inertial Oscillations during Hurricanes

4.1.1 Surface Currents during Hurricanes

Hurricanes in this study had different intensities and tracks. The distance between the hurricane center and the mooring position also varies. Thus, different hurricanes had different effect at the mooring site. Fig. 4-1 is a demonstration of the surface currents during those hurricanes and tropical storms. The current velocity was larger than 1.2m/s during Tropical Storm Arlene and larger than 0.8 m/s during Hurricane Cindy. However, when comparing with currents during Hurricane Katrina, we find that the currents during Arlene were even larger. Since we already know that Hurricane Katrina was much closer to the mooring and had much higher intensity when passing the mooring, it is reasonable to consider that the large currents during Arlene were induced by other effects, like Loop Current, which will be revisited in Section 4.4. The currents during Hurricanes Dennis and Wilma were weaker, comparing those during other hurricanes.

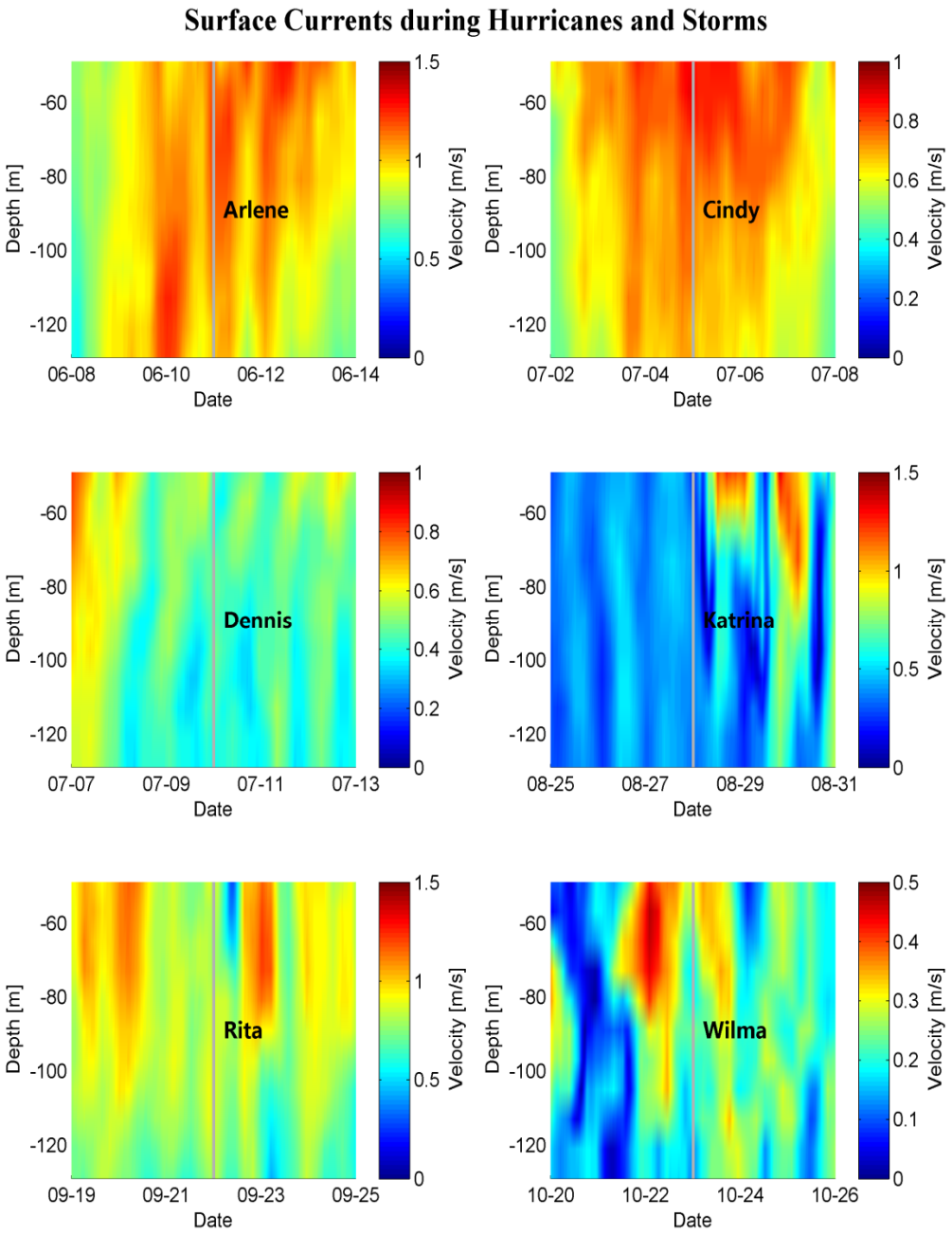

Figure 4-1 Surface Currents Raw Data during Hurricanes and Storms
(The gray line indicates the beginning of the day when hurricane was closest to the mooring. It is not necessary that the gray line itself indicates when hurricane was closest to the mooring.)

In order to identify hurricane induced near inertial oscillations excluding the effects of low frequency components like Loop Current, we apply a 40-hour high pass to the raw data. The results are presented in Fig.4-2.

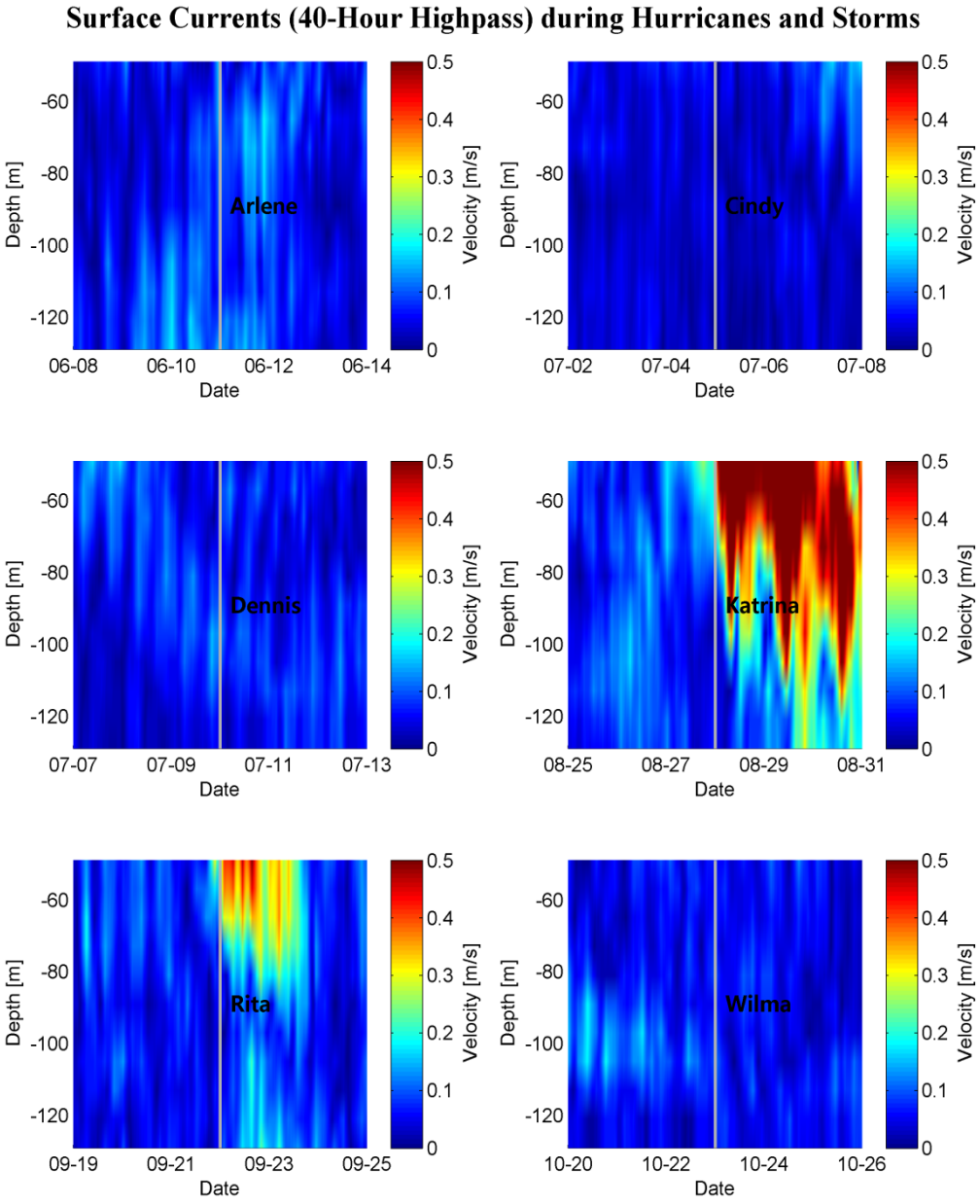

Figure 4-2 Surface Currents (after 40- Hour Highpass) during Hurricanes and Storms

We find that after the high pass filtering, the large currents existed during Hurricanes Arlene and Cindy disappeared, which indicates that the large currents during these time periods were not within the inertial oscillation band which might be induced mainly by other mechanisms such as the Loop Current. In contrast, Hurricanes Katrina and Rita generated very significant (>0.5m/s) near inertial oscillations. The near inertial oscillations during Katrina were stronger than those during Rita, though the intensity of Rita was stronger when it approached the mooring. This shows that the distance between the mooring and the hurricane center affects the strengths of hurricane induced near inertial oscillations.

The 40-hour high pass filtered currents contain all the near inertial oscillations. To better describe the near inertial oscillations which rotate clockwise with equal amplitude for *u* and *v* components, we present the current vectors in Fig.4-3. From this figure, we find several interesting facts about these near inertial oscillations: 1) The magnitudes of near inertial oscillations generated by each storm event were following this order: Katrina (197.29m^2/s^2)> Rita (35.1329 m^2/s^2) > Arlene (9.71 m^2/s^2)> Wilma (8.36 m^2/s^2)> Dennis (5.55 m^2/s^2)> Cindy (4.26 m^2/s^2) (The energy is estimated by the summation of the square of the velocity in the surface layer during the following 3 inertial period after the approaching of the storms). This is consistent with the order of the closest distance between hurricane center and the mooring (Tab. 2-1), except for Wilma and Dennis. Comparing to Wilma, Dennis was closer to the mooring and stronger when approaching the mooring. However, the near inertial energy during Wilma was slightly stronger than that during Dennis. 2) Except Cindy and Wilma, during all the other storms and hurricanes, there was significant downward propagation of near inertial energy in the surface layer, though with different patterns. 3) In Fig.4-4, we find that the surface near inertial oscillations during Katrina lasted for 4-5 inertial periods (the length of the local inertial period is indicated by the red line) and then almost disappeared; the near inertial oscillations during Rita lasted for 2 inertial periods, then disappeared for 1 inertial periods and occurred again for 7 inertial periods. However, we cannot be sure the re-occurred near inertial oscillations are directly associated with Hurricane Rita.

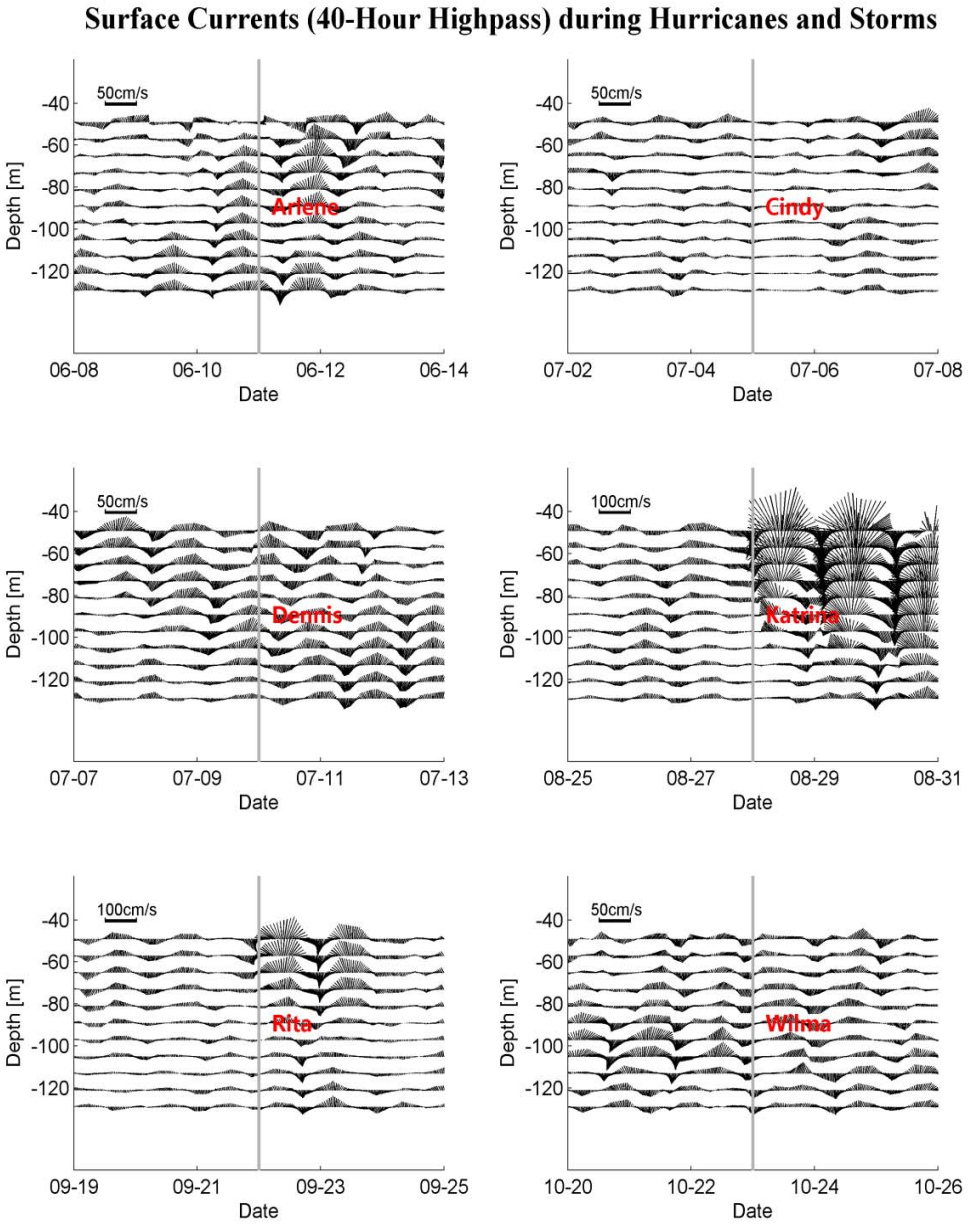

Figure 4-3 Surface Current Vectors (after 40- Hour Highpass) during Hurricanes and Storms (Notice that the unit length for Katrina and Rita is different from that for other storms)

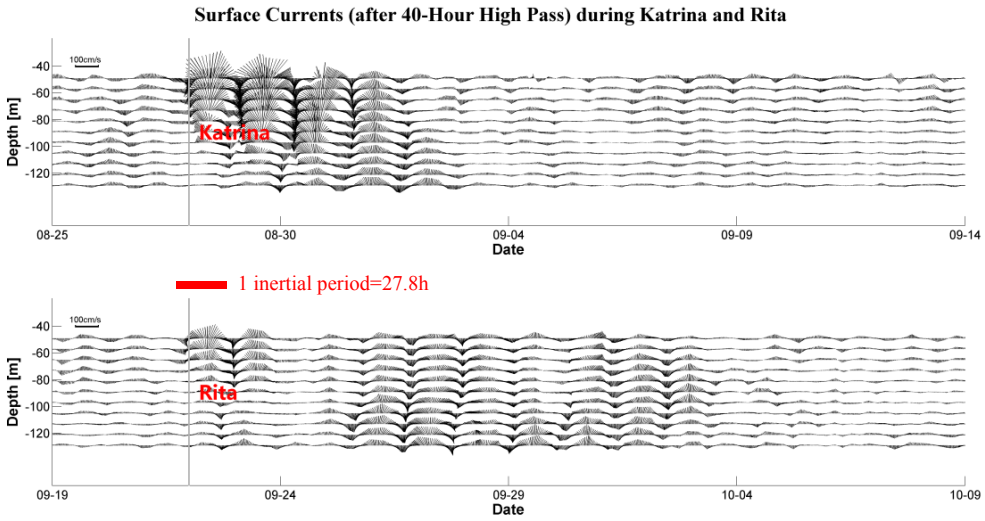

Figure 4-4 Surface Currents (after 40-Hour High Pass) during Katrina and Rita

4.1.2 Frequencies and Energy of Surface Near Inertial Oscillations during Hurricanes

The data we used here has been de-tided and filtered by 40-hour high pass. The rotary spectra are based on the data from upper most bin of the ADCP (49m depth). The power density contours are from the surface ADCP data (from 129m to 49m) through rotary spectra of different depths. Only the power densities of clockwise component are included in the power density contours. The time periods we used to do the rotary spectra analysis start from when each hurricane was closest to the mooring to 6 days later (time lengths are 6 days). Notice that in the rotary spectra, the scale of the vertical axis for Arlene, Cindy, Dennis and Wilma (0.1) is different from that for Katrina and Rita (0.4).

Arlene: The frequency corresponding to the highest peak is 0.0461cph from the rotary spectra (Fig.4-5). It is a blue shift to the local inertial frequency (f) (0.0461>0.036cph). The variations of near inertial energy (E) and frequencies (F) with depth are presented in Fig.4-6. It seems that there were 2 major peaks near the local inertial frequency. One was higher than the local *f* and it existed through the whole surface column. The other was lower than *f* and it just existed between 50m and 90m depths.

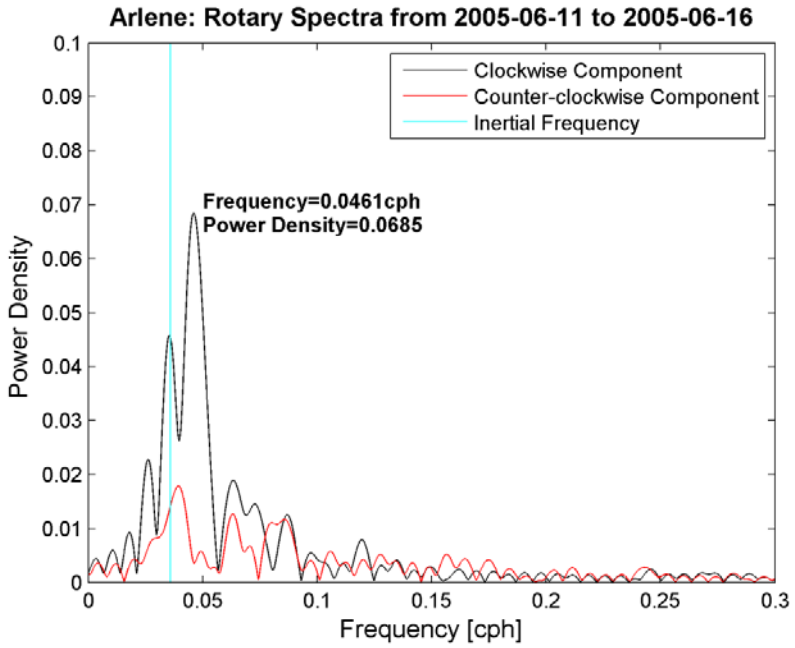

Figure 4-5 Rotary Spectra for Arlene

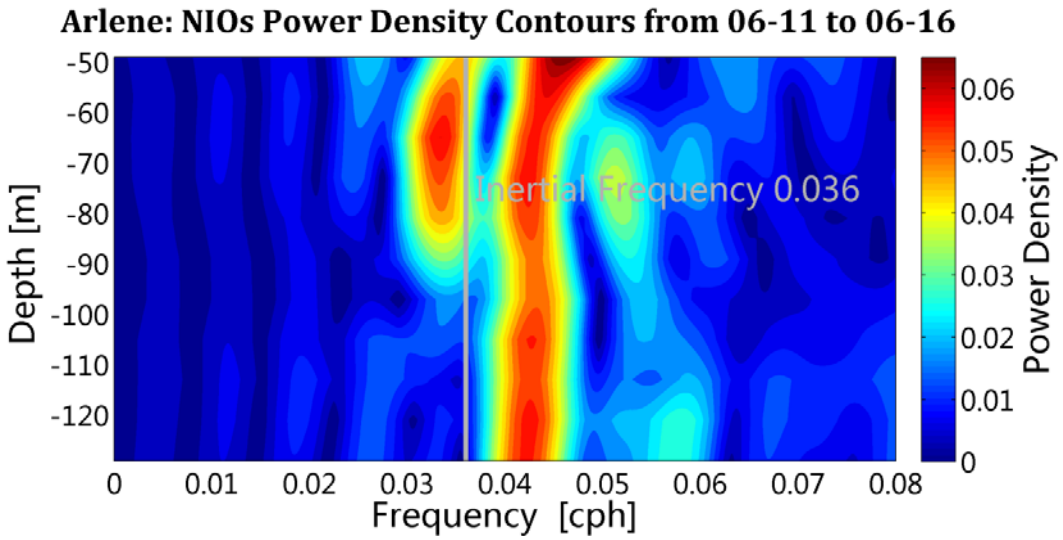

Figure 4-6 NIOs Power Density Contours during Arlene

Cindy: There was also a blue shift to the local inertial frequency in the rotary spectra (0.0379 >0.036cph) (Fig. 4-7). In the upper part of the surface layer (higher than 70m depth), the power density was much stronger than that of the lower part. The high power density peak in the upper part seems to have separated into 2 weaker peaks in the low part (Fig. 4-8).

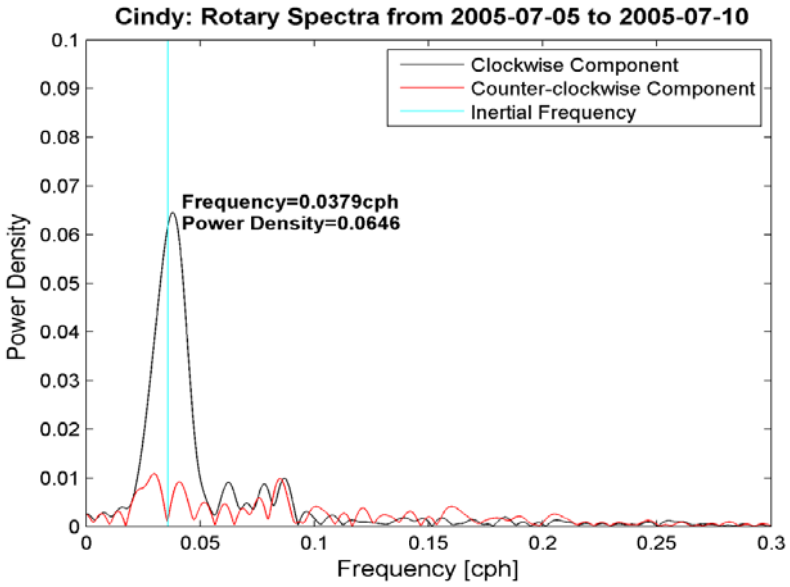

Figure 4-7 Rotary Spectra for Cindy

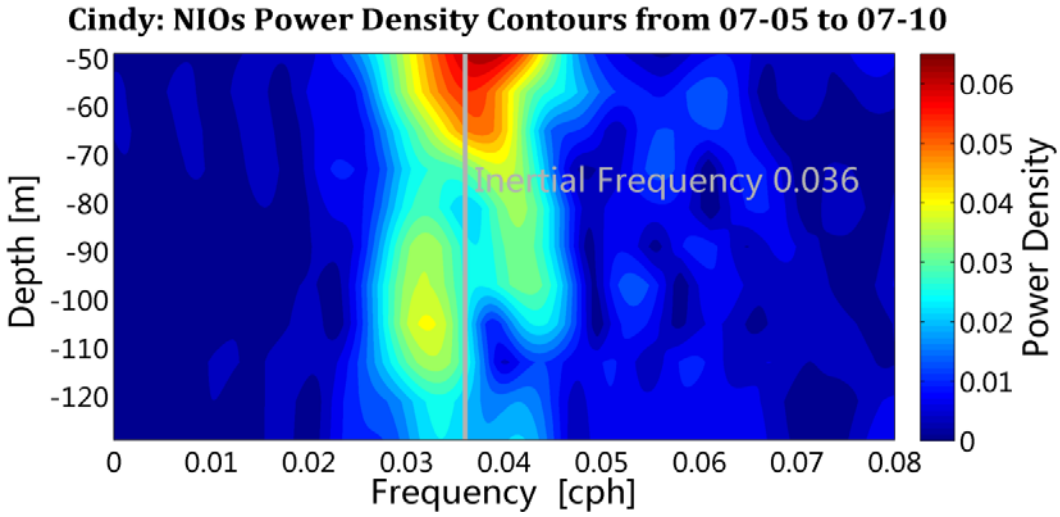

Figure 4-8 NIOs Power Density Contours during Cindy

Dennis: In the rotary spectra (Fig. 4-9), there are 2 comparable high peaks. They both have higher frequencies than the local f (blue shift). The frequency of the higher one is 0.0431cph. The power density of the middle part was stronger than the upper and lower part of the surface layer (Fig. 4-10). The two major peaks seem to exist through the surface column, while the lower frequency peak became stronger when depth increases.

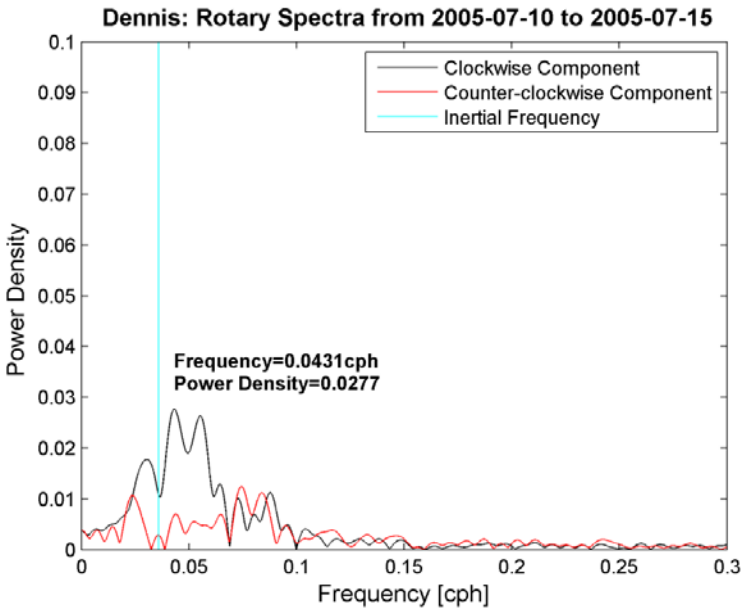

Figure 4-9 Rotary Spectra for Dennis

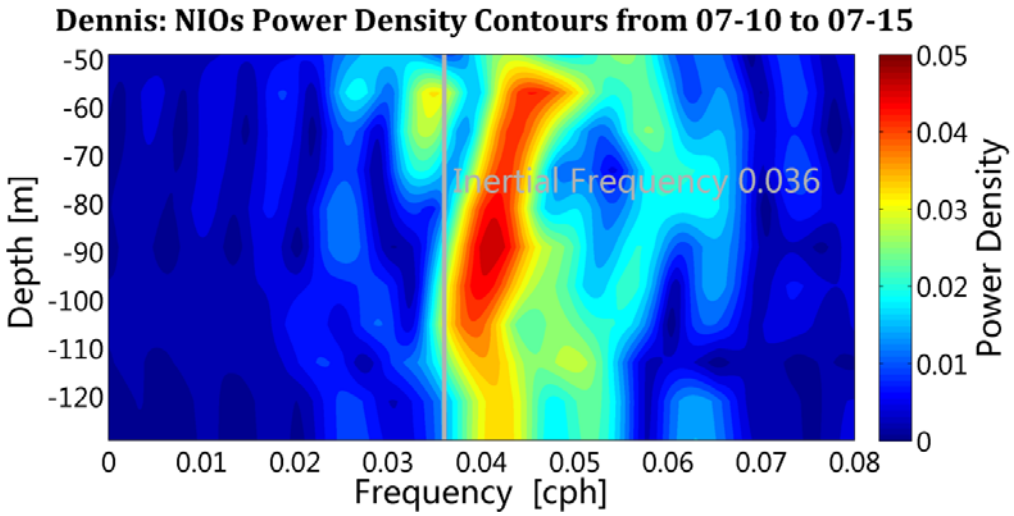

Figure 4-10 NIOs Power Density Contours during Dennis

Katrina: The near inertial oscillation frequency from the rotary spectra (Fig. 4-11) is 0.0348cph, which is a redshift. Near inertial frequencies of each layer were almost the same. Power density dropped from 0.35 of the upper part to 0.15 of the lower part (Fig. 4-12), though 0.15 is still much higher than the power density during any other storm in this study.

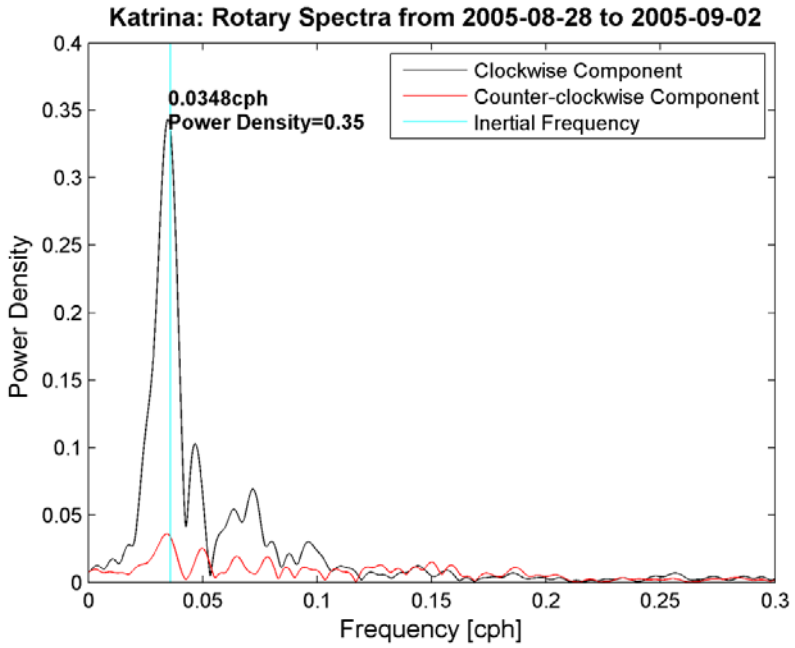

Figure 4-11 Rotary Spectra for Katrina

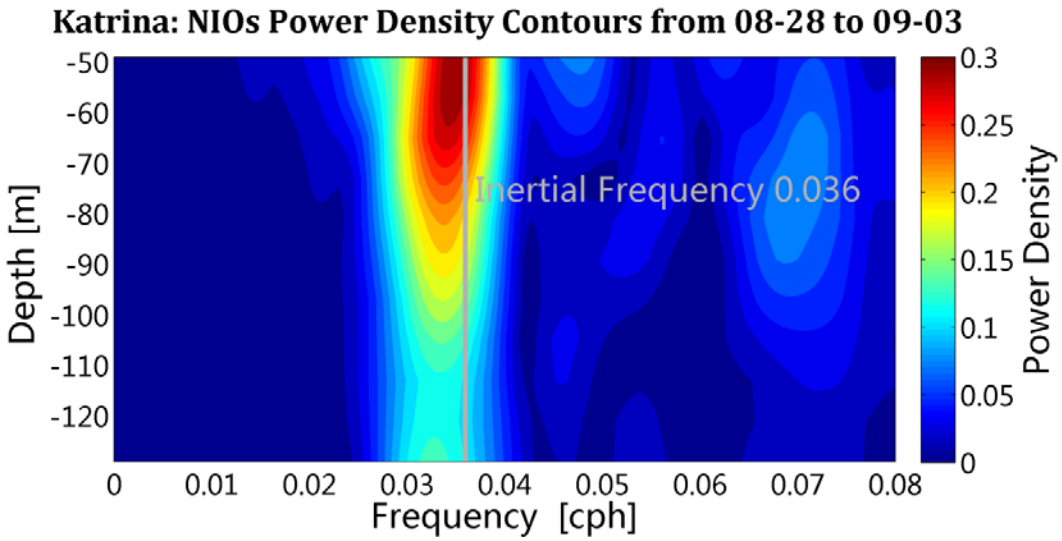

Figure 4-12 NIOs Power Density Contours during Katrina

Rita: The frequency for the surface near inertial oscillation was 0.0335cph (Fig. 4-13), which is a redshift. The near inertial oscillation frequencies of each layer were almost the same. The power density first decreased from 50m to 85m, but then increased from 85m to 110m depth (Fig. 4-14).

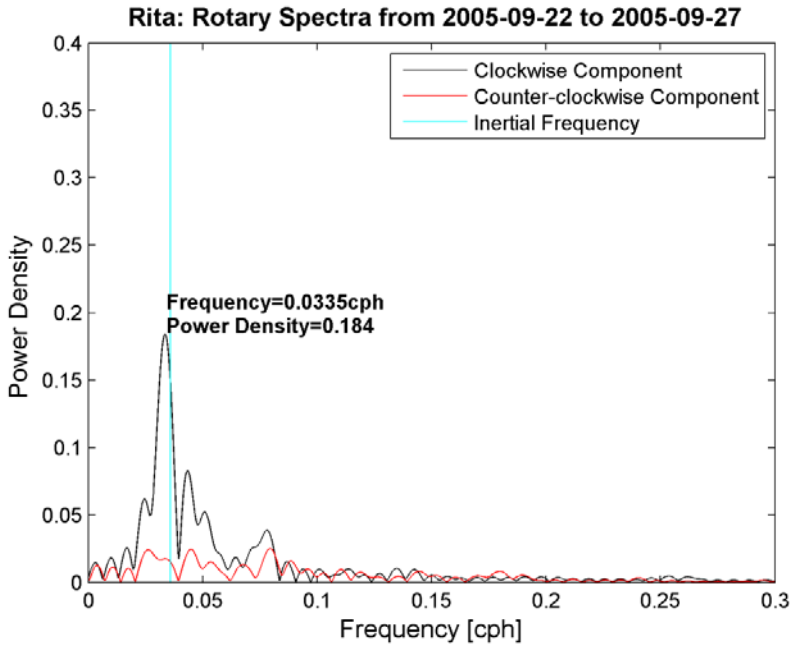

Figure 4-13 Rotary Spectra for Rita

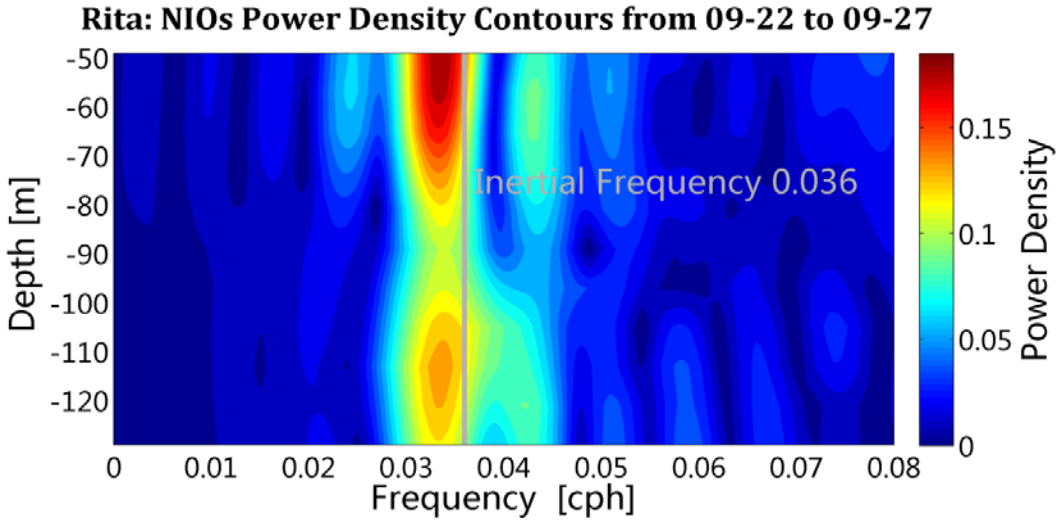

Figure 4-14 NIOs Power Density Contours during Rita

Wilma: The frequency for the surface near inertial oscillation during Wilma is 0.0366cph (Fig. 4-15), which is almost identical to the local inertial frequency (0.0366 vs. 0.036cph). The highest near inertial energy was not in the very surface but around 85m depth (Fig. 4-16).

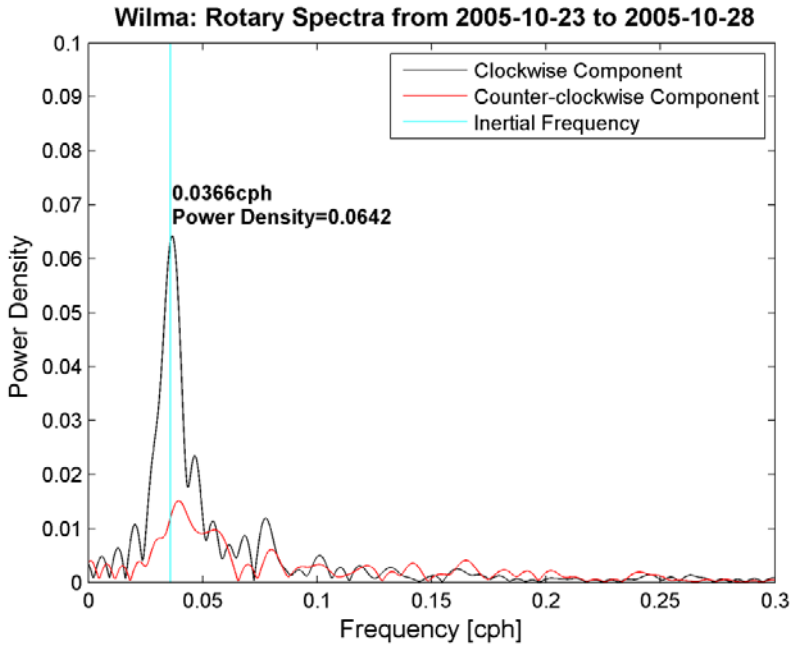

Figure 4-15 Rotary Spectra for Wilma

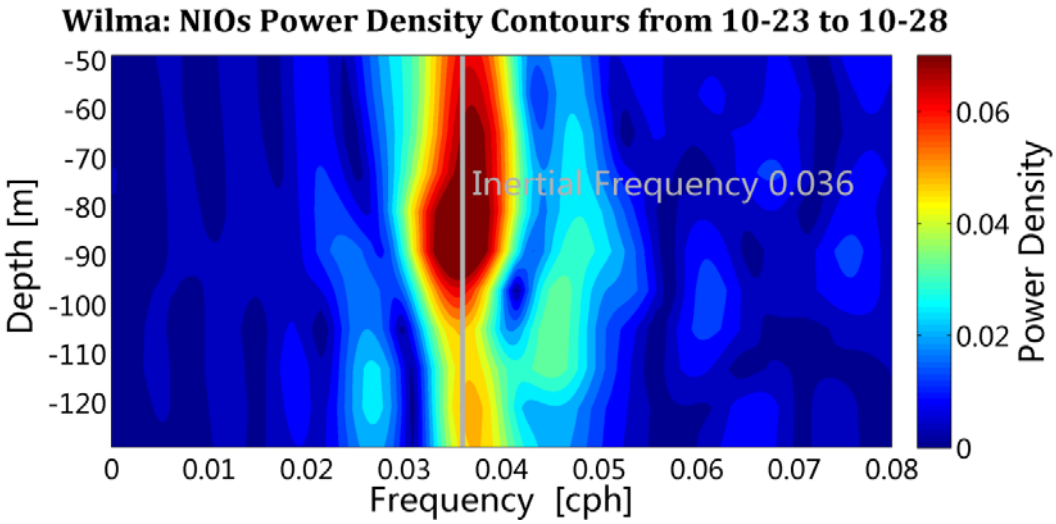

Figure 4-16 NIOs Power Density Contours during Wilma

We also use F'=f+ζ/2 (Chapter 3.9) to calculate the surface near inertial frequency (F') based on the SSH data. The comparisons of the near inertial frequency (F) from upper most bin of the ADCP and F' are listed in Table 4-1:

Table 4-1 Comparisons of F and F' during Each Hurricane

Hurricane	F (Cph, ADCP)	F' (Cph, SSH)
Arlene	0.0461	0.0353
Cindy	0.0379	0.0354
Dennis	0.0431	0.0352
Katrina	0.0348	0.0311
Rita	0.0335	0.0345
Wilma	0.0366	0.0339

We find that the vorticities have at the same order of magnitude with that of local inertial frequency. This proves that the vorticity of geostrophic flow will affect near inertial oscillations. We found a correlation between F and F' (the square of correlation coefficient, R^2) to be 0.3172. The possible explanations for the relatively low correlation could be:

1) The SSH data is not a real time data, but a combination product of multiple satellite data. Interpolations in time and space have been applied to make the SSH data. The sampling frequency of the satellite SSH data at a specific point is around 30 days. Thus, the satellite data cannot provide us with the daily change of the current, while the inertial oscillation period is around one day.

2) The near inertial oscillation frequency is related to the local vorticity, which has small scales. The vorticities calculated from the SSH data can represent larger scale dynamics better, but with errors for smaller scale near inertial oscillations.

3) Although the LSU mooring was in the Loop Current, which is conceptually a quasi-geostrophic flow. However, sometimes the change of the flow was very rapid that it no longer satisfied the quasi-geostrophic assumption. In other words, ageostrophic flow cannot be captured by SSH data using quasi-geostrophic flow assumption, which is expected.

4) The ADCP data we used to make the rotary spectra is at the depth of 49m. The quasi-geostrophic flow calculated from the SSH data just represent the very surface flow. The difference in depths can cause difference in results.

5) Most of the time, we have a single significant high peak near the inertial frequency, so that we can easily determine the near inertial oscillation frequency. However, sometimes there are several comparable high peaks in the rotary spectra; thus, the way we determine the near inertial frequency is subjective in this situation, which can cause errors.

The comparisons of the two components of the velocity from SSH and from ADCP are as Fig. 4-17:

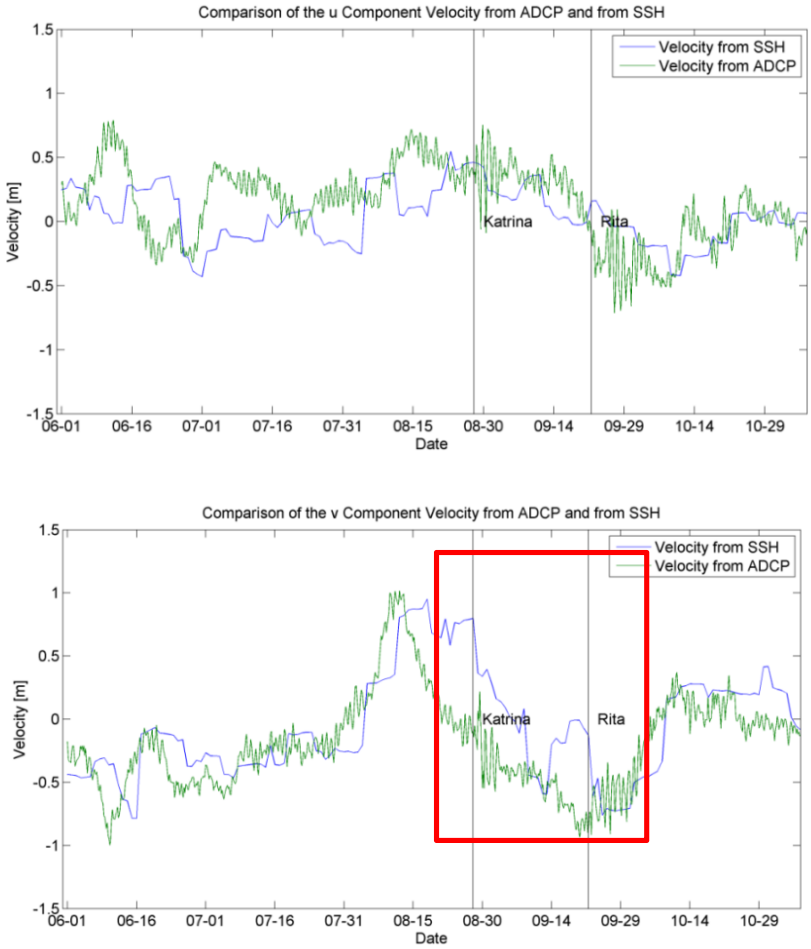

Figure 4-17 Comparisons of the Velocities from SSH and from ADCP

The R (correlation coefficient) of the *u* component is 0.3503 and the R for *v* component is 0.6534. The *v* component calculated from SSH based on quasi-geostrophic assumption is closer to the real situation. The period of time indicated by the red box in Fig. 4-17 showed a larger discrepancy between the currents calculated from SSH and measured by ADCP. The explanation may be that the rapid velocity change in this period of time violated the quasi-geostrophic assumption which requires a slow velocity variation. These rapid changes of velocity are associated with the activity of Loop Current which will be discussed in Chapter 4.4.

4.1.3 Phase Lag of Surface Near Inertial Oscillations

Comparing Fig.4-18, Fig.4-3 and Fig.4-4 (note the time ranges are not the same), we find that when there were significant near inertial oscillations through the whole surface water column, the phases through the surface column at the same time seemed to be uniform (Katrina: 8/31 to 9/2 and Rita: 9/27 to 9/28). After zooming in the phase variations during these 2 time periods in Fig. 4-19 and comparing it with the current velocity vector time series (Fig. 4-20, after 40-hour highpass and de-tided), we find that the phase propagation is from the bottom to the surface. The averaged phase speed during Katrina was 0.56cm/s, while during Rita, the speed was higher than 2cm/s.

The white and red arrows in Fig.4-16 and Fig.4-17 denote the downward propagations of "disturbances" (inconsistent phase with that of surrounding depths). Comparing Fig.4-16 and Fig.4-17, we find that in the lower part of the surface layer, the amplitudes of near inertial oscillations were much smaller than those in the upper part. From the rotary spectra of the currents at the 97m below the surface with these disturbances from 08/28/2005 00:00 to 08/30/2005 00:00 and from 09/22/2005 00:00 to 09/24/2005 00:00, respectively (Fig.4-21), we can tell that the disturbances were caused by the interaction of near inertial oscillations and higher frequency components of currents. The phases of the higher frequency current interfere with the phases of near inertial oscillations. This process also cause the decrease of the near inertial oscillation amplitude.

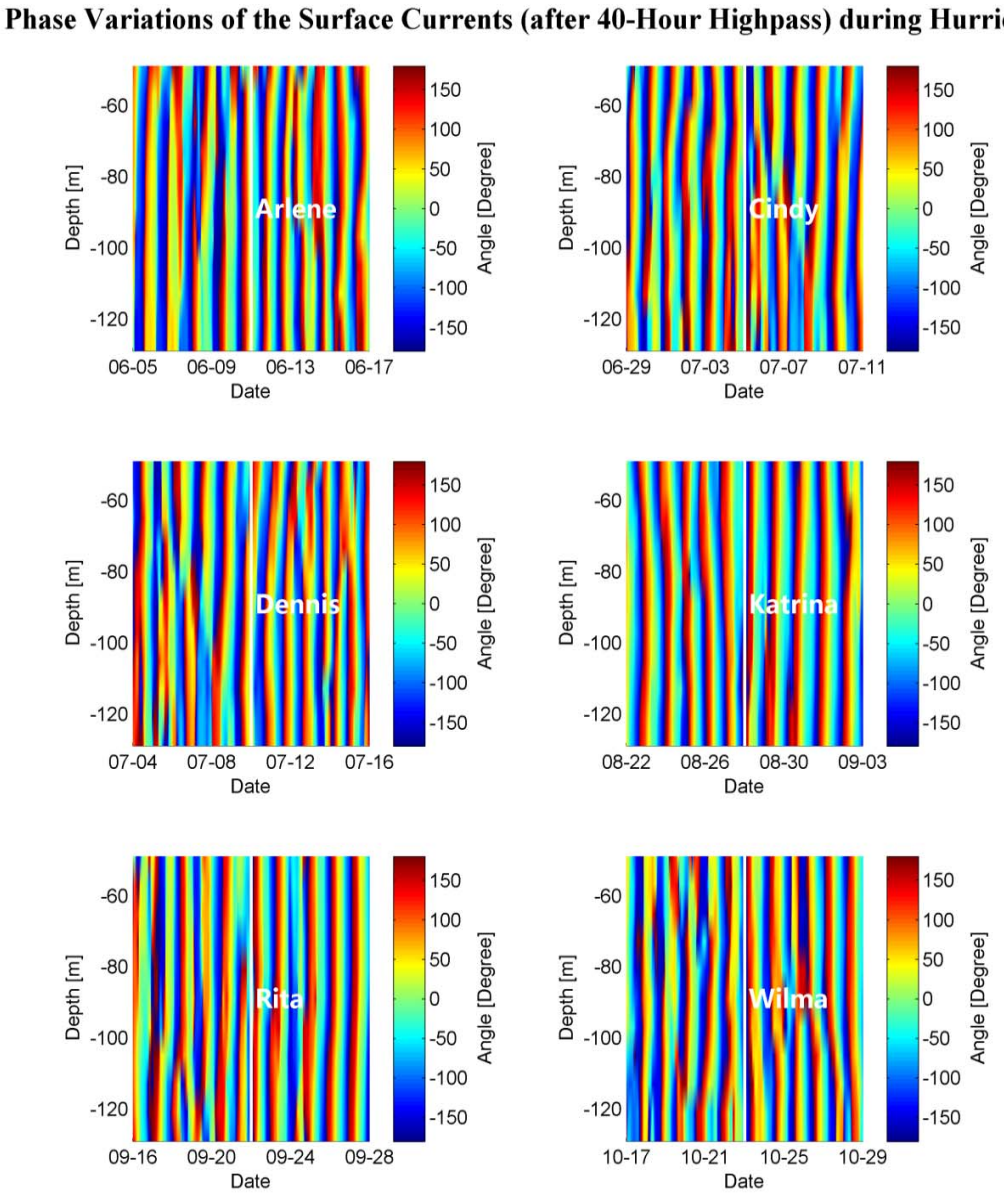

Figure 4-18 Phase Variations of the Surface Currents (after 40-Hour Highpass) during Hurricanes

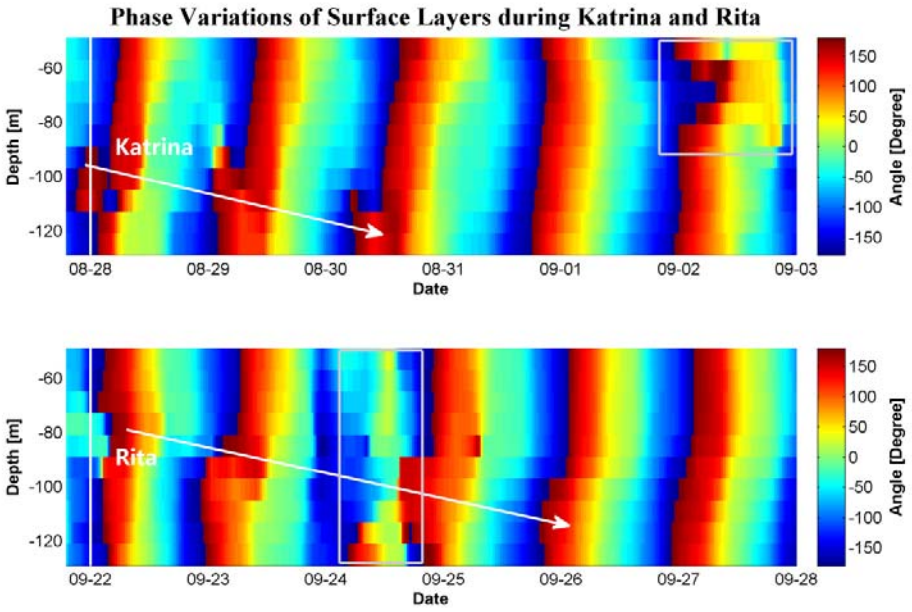

Figure 4-19 Phase Variations of Surface Layers during Katrina and Rita (The color of a specific layer represents the angle of the bottom of that layer)

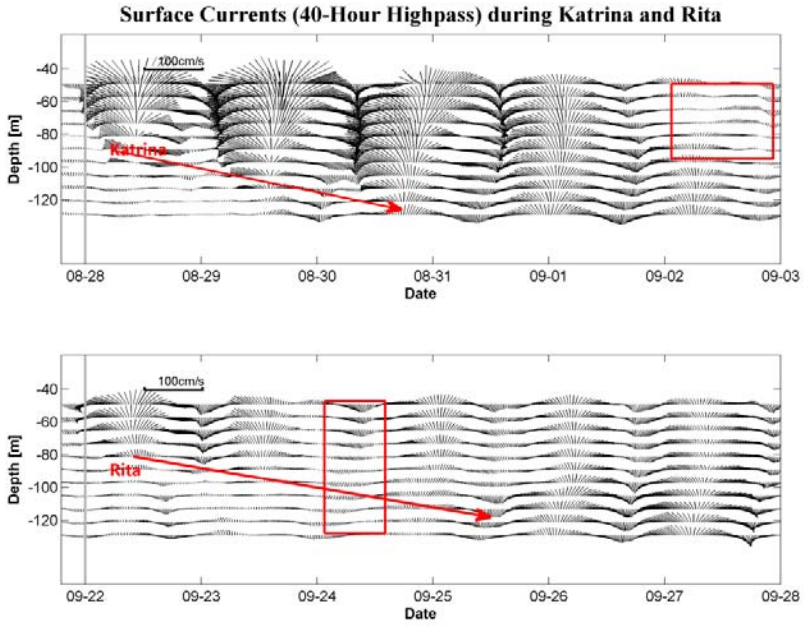

Figure 4-20 Surface Currents during Katrina and Rita

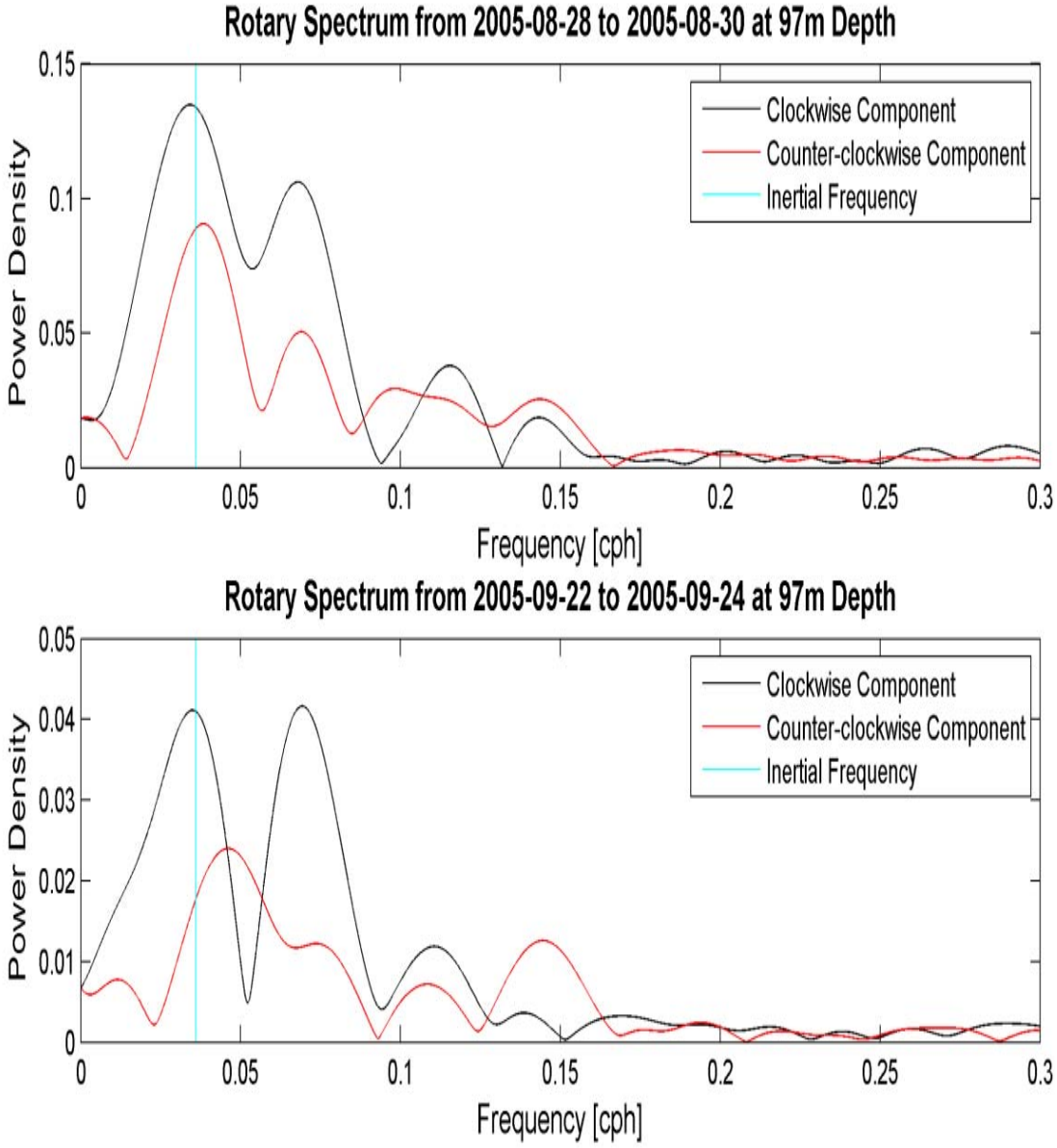

Figure 4-21 Rotary Spectra for Disturbances

4.2 Mid-layer Near Inertial Oscillations during Hurricanes and Storms

4.2.1 Mid-layer Tide Residual Currents during Hurricanes and Storms

The mid-layer is from 200m depth to 1500m depth. In Fig. 4-22, the tide components in the currents have been eliminated. The strong currents in the figure, from 200m to 400m depth, are from the Loop Current.

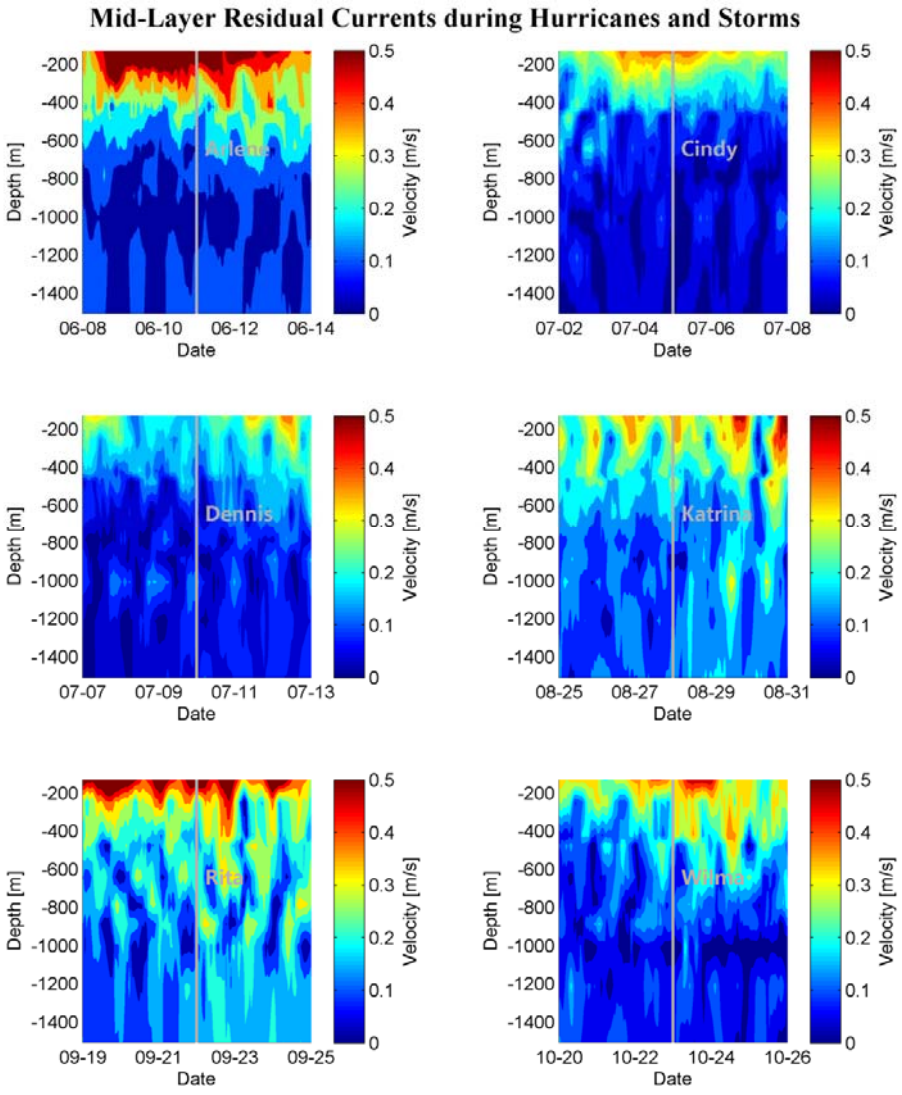

Figure 4-22 Mid-Layer Residual Currents during Hurricanes and Storms

4.2.2 Mid-layer Inertial Oscillations during Hurricanes and Storms

From Fig.4-23 and Fig.4-24, we can see that in mid-layers, there were also near inertial oscillations. However, we do not see any vertical propagation of near inertial oscillations except during Katrina (Fig. 4-23, Fig. 4-25), since they appear random both in phase and magnitude at different depths.

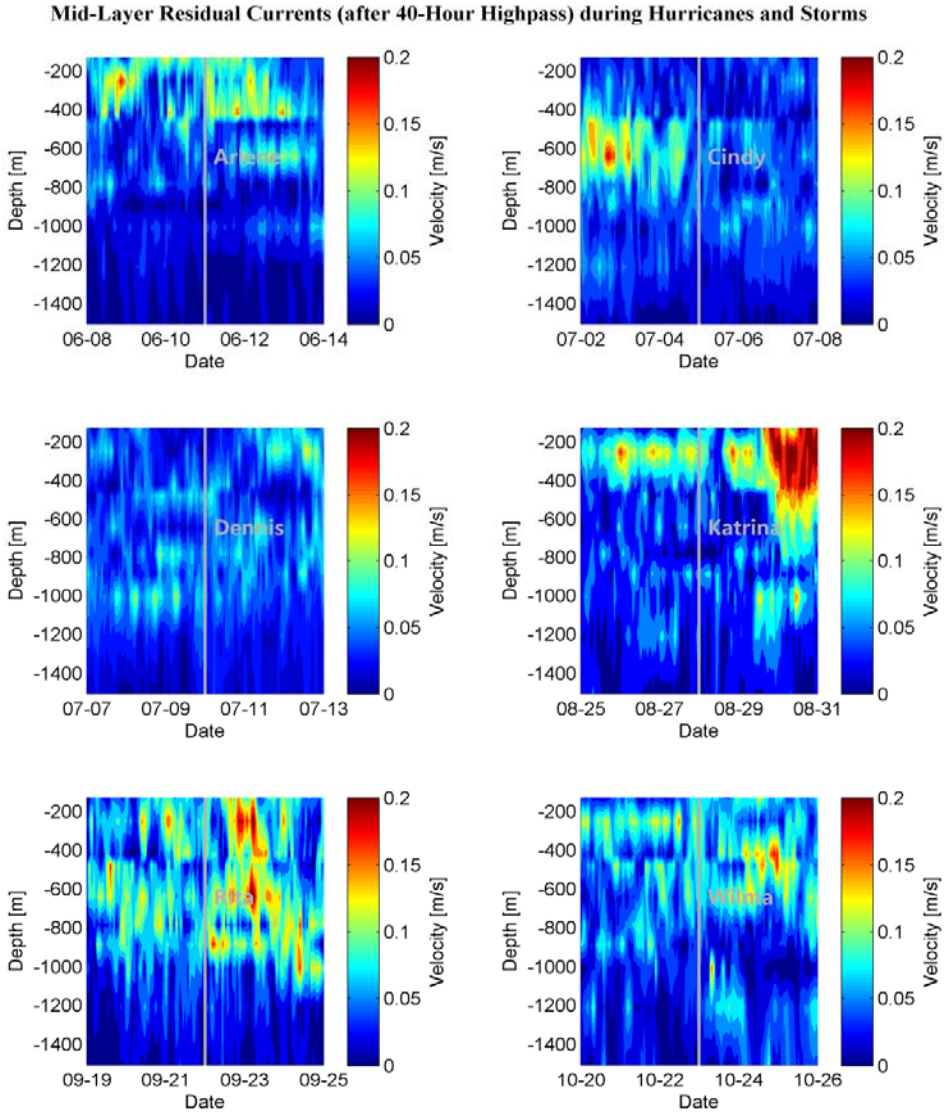

Figure 4-23 Mid-Layer Residual Currents (after 40-Hour Highpass) during Hurricanes and Storms

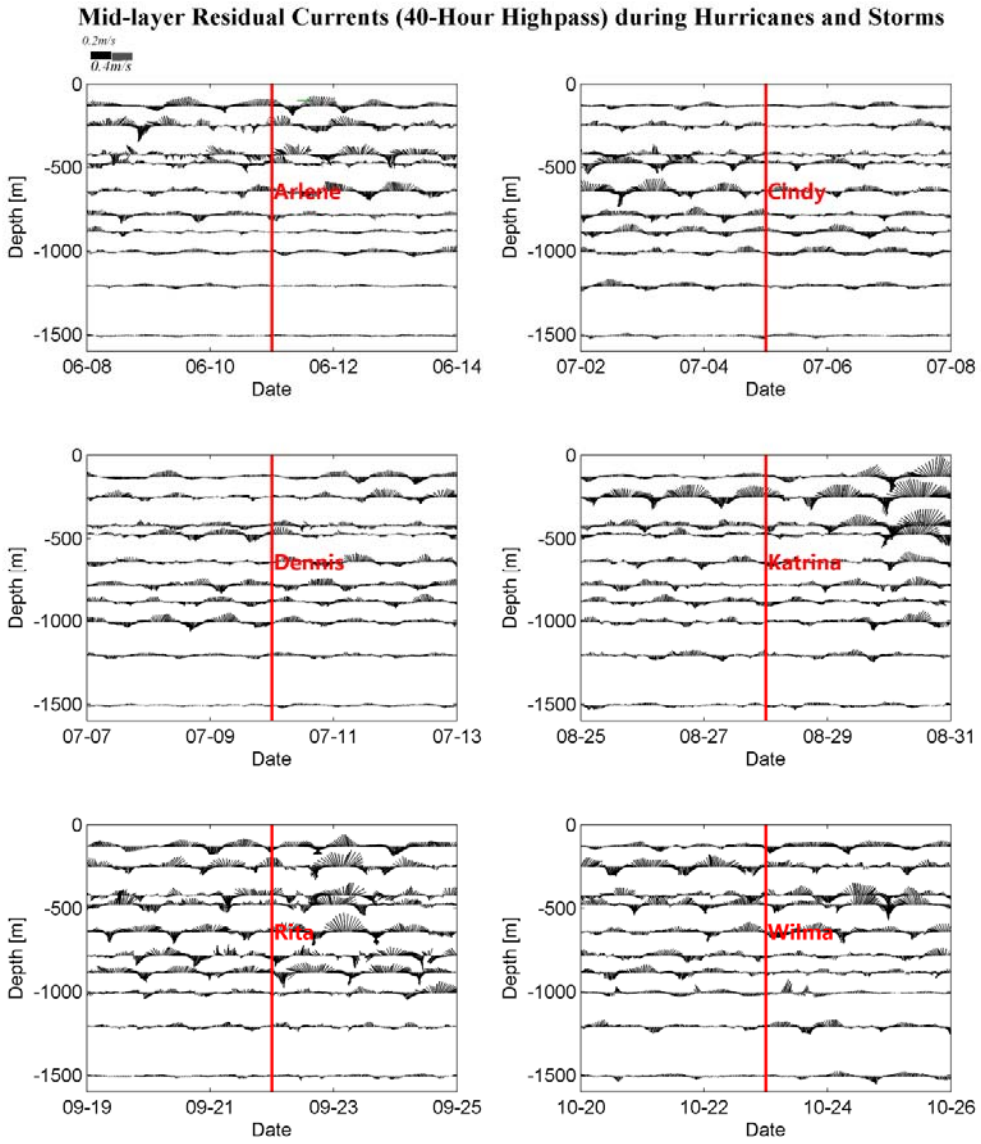

Figure 4-24 Mid-Layer Residual Currents (after 40-Hour Highpass) during Hurricanes and Storms

4.2.3 Vertical Propagation of Near Inertial Oscillation Energy between Surface Layer and Mid-Layer during Katrina

The near inertial energy in Fig.4-25 is proportional to the squared velocity which is after a 15-40 hour bandpass filter. We can see that the high near inertial energy transferred downward from surface to 800m depth. It is interesting that there seems to be reflections in the mid-layer as demonstrated in Fig.4-25. The

near inertial oscillations transferred from surface to around 450m depth. Then part of it reflected back to around 200m depth (where thermocline was), the other part of it went down until around 800m depth. It then reflected back again to around 450m depth. The energy around 200m was relatively lower, while comparing with Fig. 2-5, the 200m and 800m depths correspond to the salinity and temperature stratification depths (Oey and Wang, 2009; Welsh et al., 2008; Shcherbina et al., 2002).

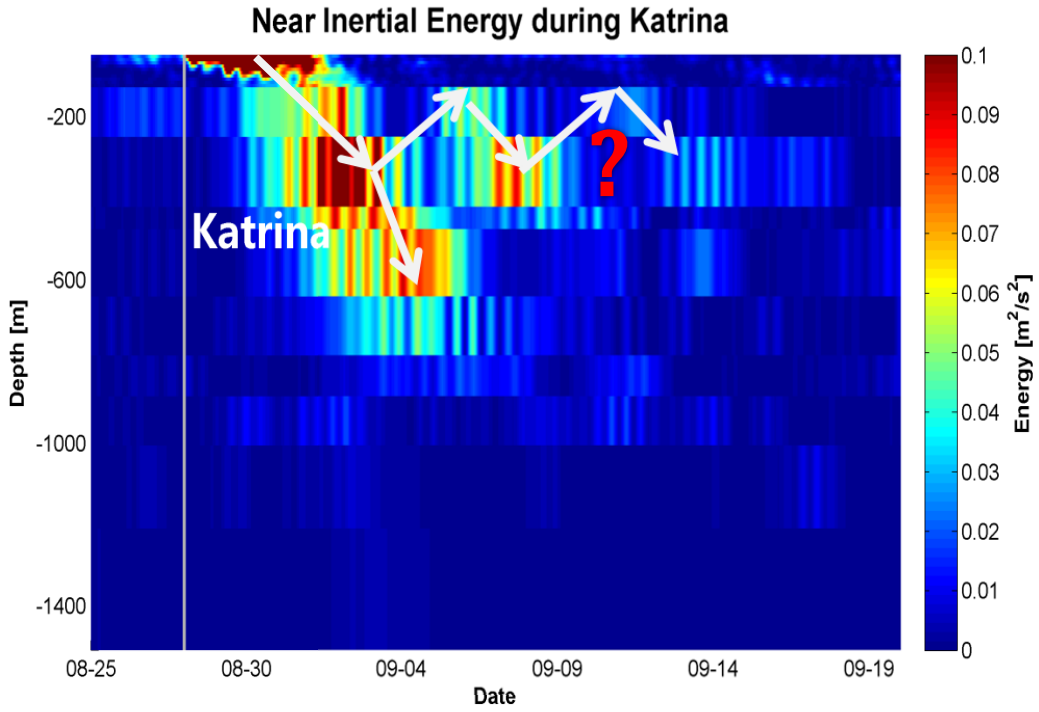

Figure 4-25 Near Inertial Energy during Katrina (The color of a specific rectangle represents the energy at the bottom depth of that rectangle)

To quantify the downward propagation of the near inertial oscillation energy, we assume that the highest near inertial oscillation energy at each depth is caused by the same event, so that we can track the downward propagation of the near inertial oscillations. The downward propagation track based on this assumption is shown in Fig. 4-26 as the white line. In Fig. 4-26, we have modified the scale of the color bar to better indicate the highest near inertial oscillation energy of each layer.

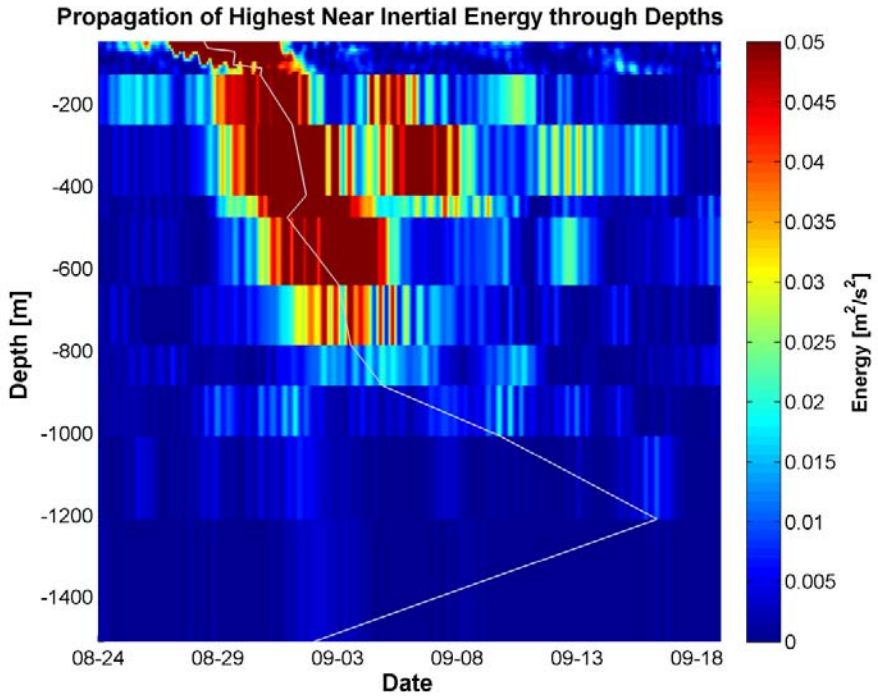

Figure 4-26 Propagation of Highest Near Inertial Energy through Vertical Profile (The color of a specific rectangular represents the energy of the bottom of that rectangular)

The slope of each segment of the white line demonstrates the downward propagating speed. We can roughly separate the white line into 4 parts: surface (49m) to 200m, 200m to 800m, 800m to 1200m and 1200m to 1400m or even deeper. It took near inertial oscillations 88hours to penetrate the first layer of 151m thickness (the group speed is 0.047cm/s); 58.5 hours for the second layer of 535m thickness (the group speed is 0.25cm/s); 307 hours for the third layer of 614m thickness (the group speed is 0.038cm/s). The highest near inertial energy of the forth layer appears much earlier than the above layer. This indicates that there is little connection between the surface and bottom near inertial oscillations. Since even huge near inertial oscillations generated by Katrina cannot directly affect this depth, we can conclude that we can hardly find large near inertial energy transferring from surface to this depth at this site. Fig.4-27 shows how near inertial energy decreased through depths based on the above assumption. We find that the near inertial energy decreased with depth exponentially as the red line indicated.

With Curve Fitting Tool from Matlab, we find the energy and the depth satisfy the function: $\text{Energy} = 1.19 * \exp(0.012 * \text{Depth})$ (Depth is negative), with 95% confidence bounds. The Correlation Coefficient Square is 0.84.

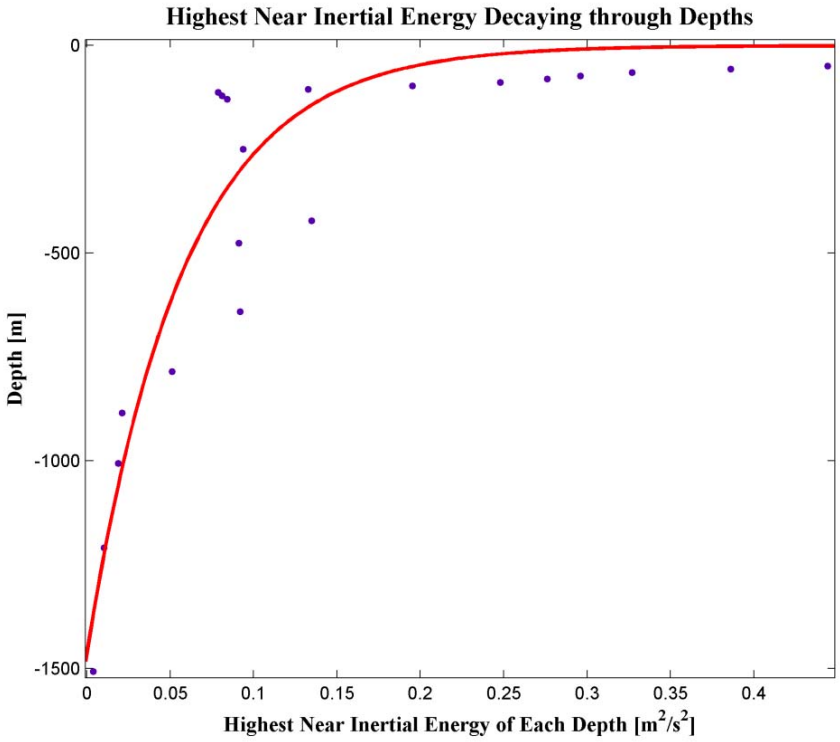

Figure 4-27 Highest Near Inertial Energy Decaying through Depths

4.3 Bottom Near inertial Oscillations during Hurricanes and Storms

4.3.1 Bottom Currents during Hurricanes

In order to find how hurricanes can affect bottom water, we present the tidal residual and tidal residual after 40 hour highpass in Fig.4-28 and Fig.4-29. It seems that the relatively high energy after Katrina in Fig.4-29 was associated with Katrina, since there is a sharp contrast of the high frequency energy between before Katrina and after Katrina. In Chapter 4.2.2, we have mentioned that the surface generated downward propagation of near inertial energy almost disappeared after 1200m depth, implying that the response of near inertial oscillation energy to Katrina in the bottom layer was much ahead of the mid-layers. The explanation is that the generation of near inertial oscillation at the bottom layer is through barotropic processes.

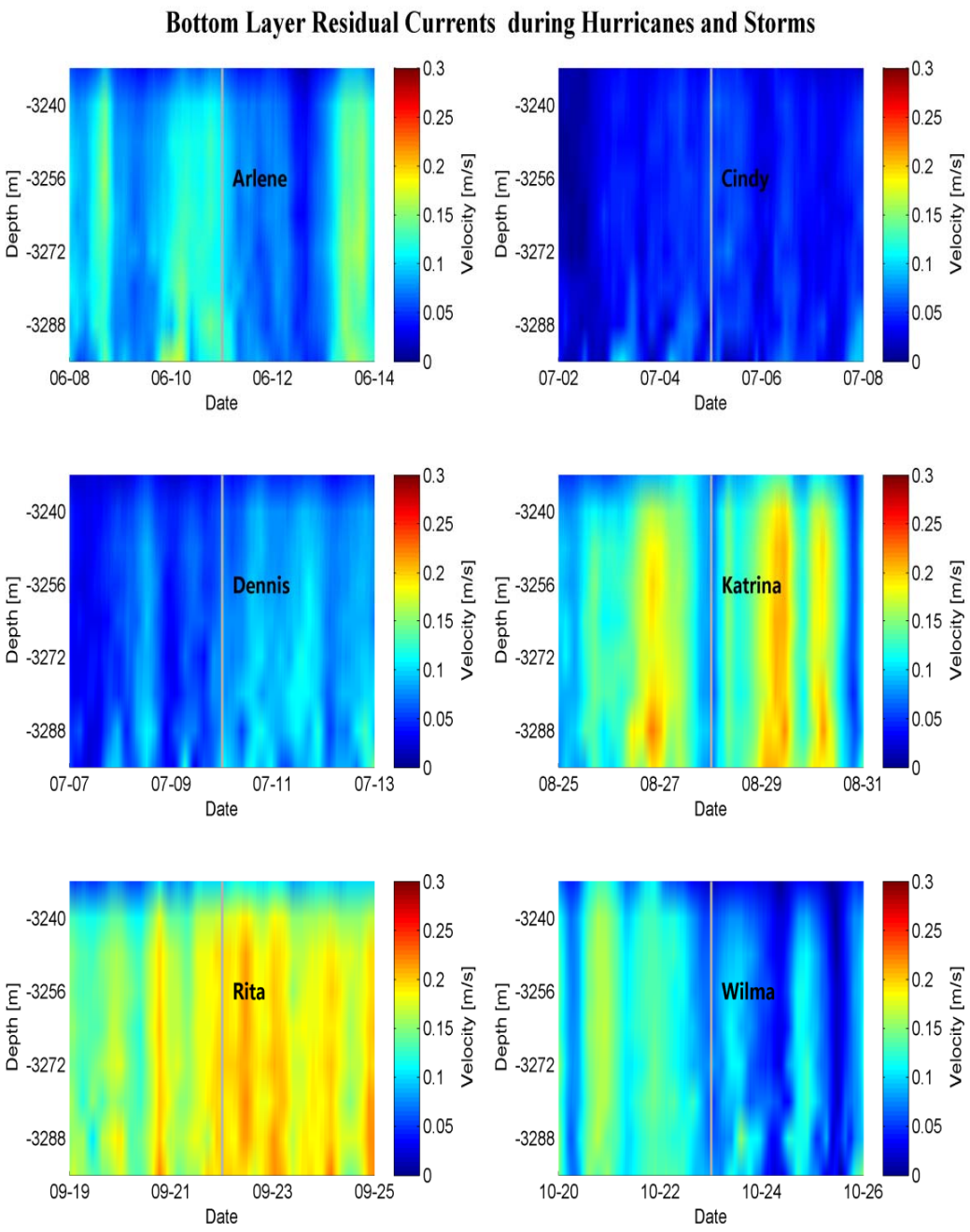

Figure 4-28 Bottom Layer Tidal Residual Currents during Hurricanes and Storms

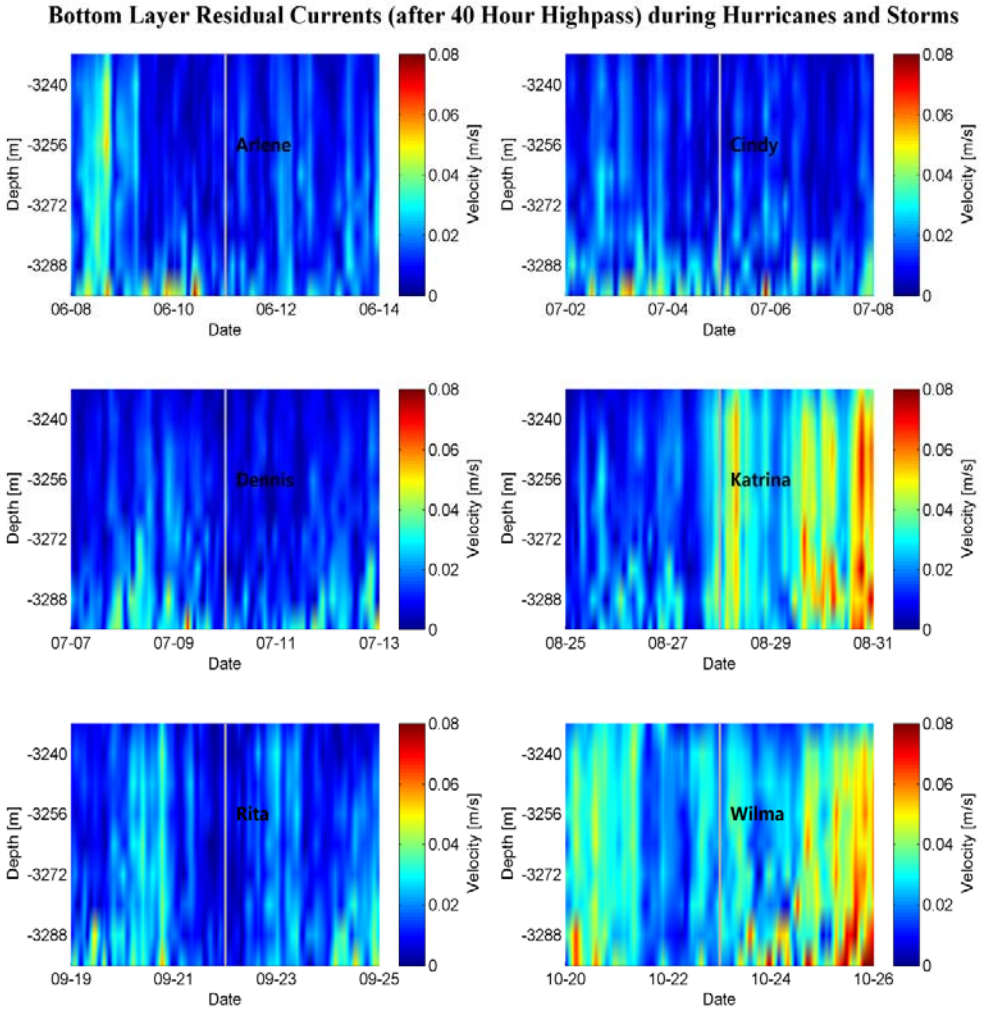

Figure 4-29 Bottom Layer Tidal Residual (after 40 Hour Highpass) Currents during Hurricanes and Storms

In contrast, the downward propagation of near inertial energy in the surface 1200m is mainly through baroclinic processes. As a result, in the surface layer, the near inertial oscillations went down slowly but in the bottom they occurred almost immediately after Katrina. This is presented in Fig.4-30.

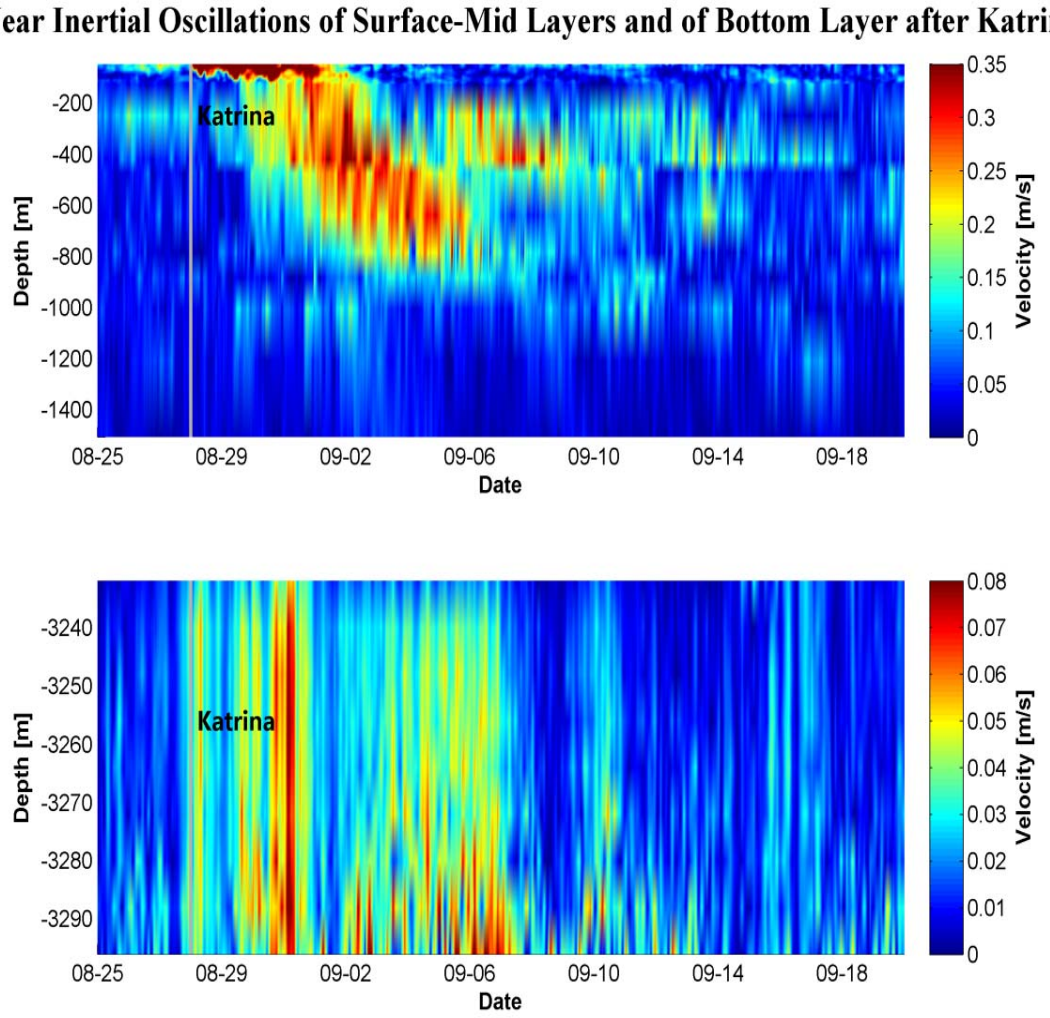

Figure 4-30 Near Inertial Oscillations of Surface-Mid Layers and of Bottom Layer after Katrina

4.3.2 Phase Lag of Near Inertial Oscillations in the Bottom Layer during Storms and Hurricanes

Fig.4-31 presents the phase variations of near inertial oscillations in the bottom layers. We find that the phases during Arlene, Cindy, Rita and Dennis were complicated and the data quality does not allow a quantification of the vertical propagation. The phases during Wilma were more "regular". Only the after Katrina did the phase variation seem to be more uniform and less random.

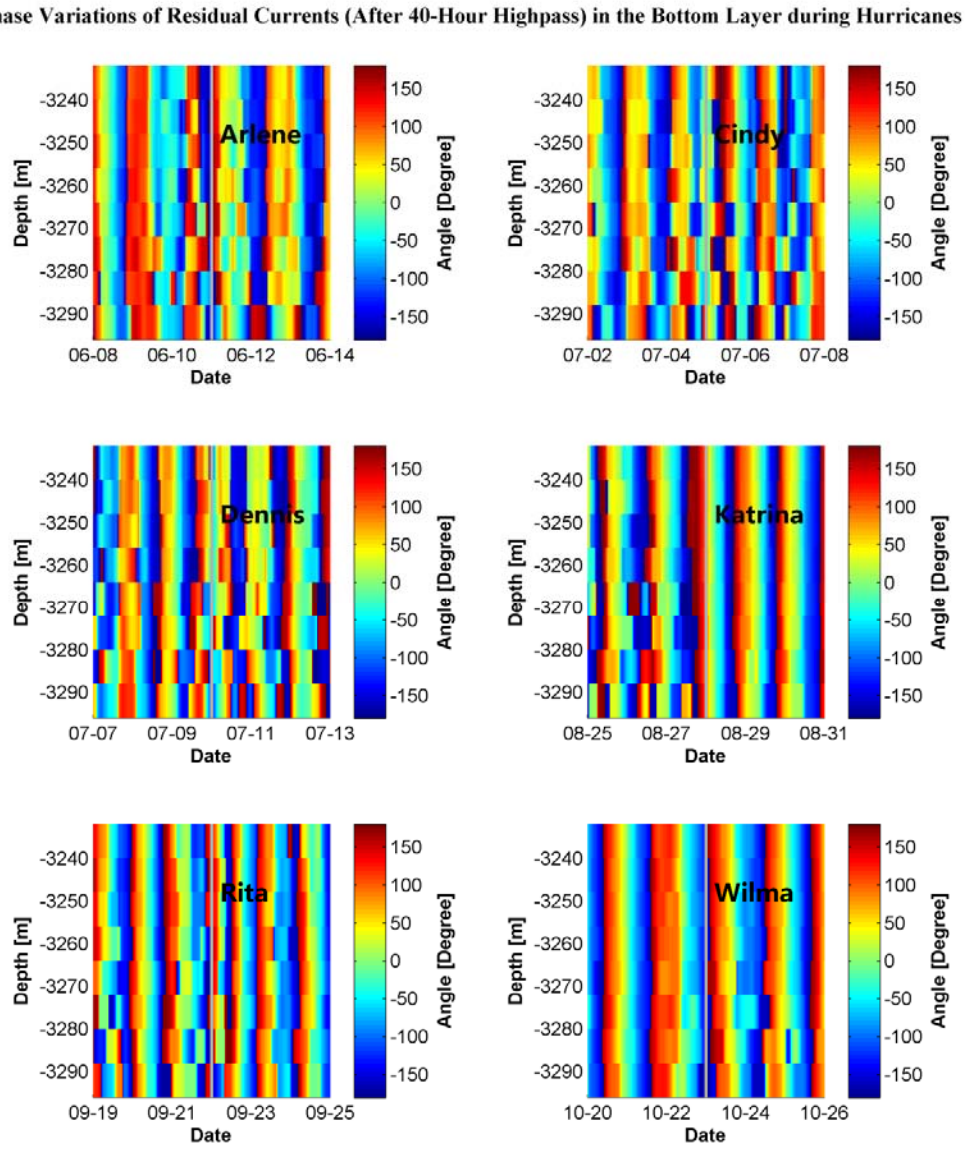

Figure 4-31 Phase Variations of Residual Currents (After 40-Hour Highpass) in the Bottom Layer during Hurricanes

The phase differences between the top and bottom of the bottom layer during Katrina were too small to evaluate the phase velocity. This is also due to the fact that the near inertial oscillations in the bottom layer propagated very fast through barotropic processes.

4.4 Surface Near Inertial Oscillations and Surface Wind

4.4.1 Surface Wind

Fig.4-32 shows the wind of two buoys (Buoy 42001 and Buoy 42003) during the research period of time. Since Buoy 42001 was closer to the track of Rita than Katrina, the wind strength of Rita was much stronger than Katrina in its records. The two panels of Fig.4-33 are the wind roses for the wind recorded by the 2 buoys. The directions are the directions where the wind blowed to. We find that most of the wind is blowing to the west or southwest direction (east or northeast wind), which is consistent with the direction of Trade Wind around this latitude.

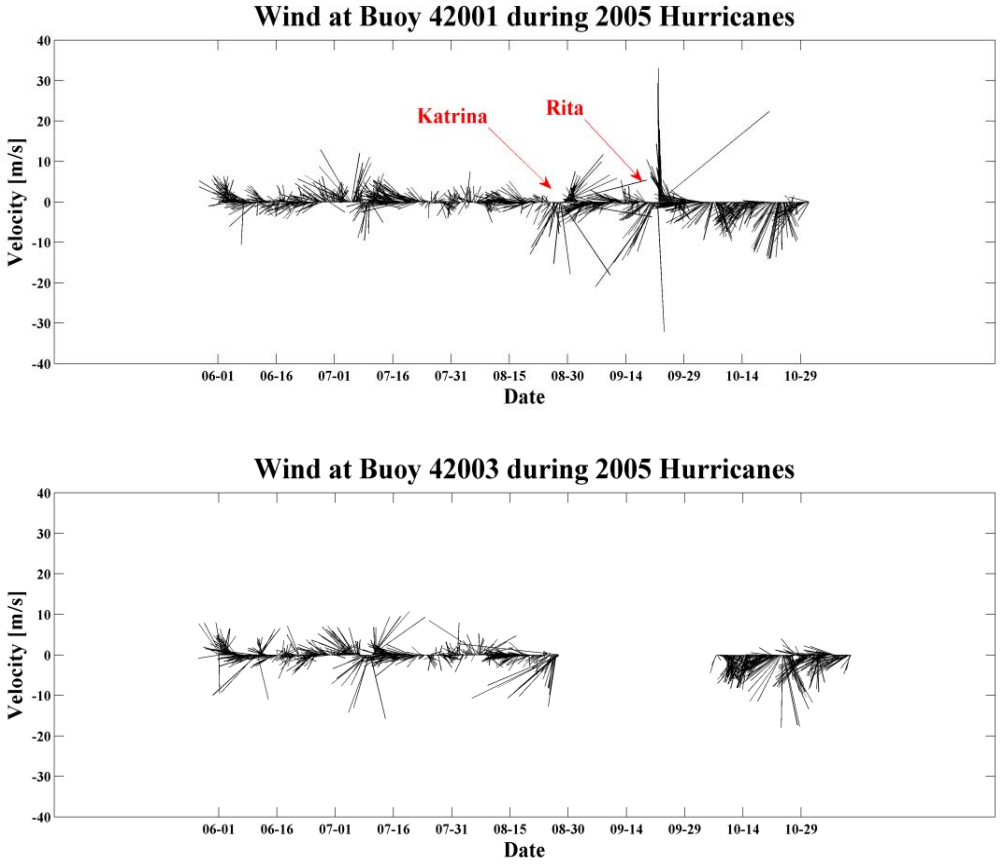

Figure 4-32 Wind at 2 Buoys

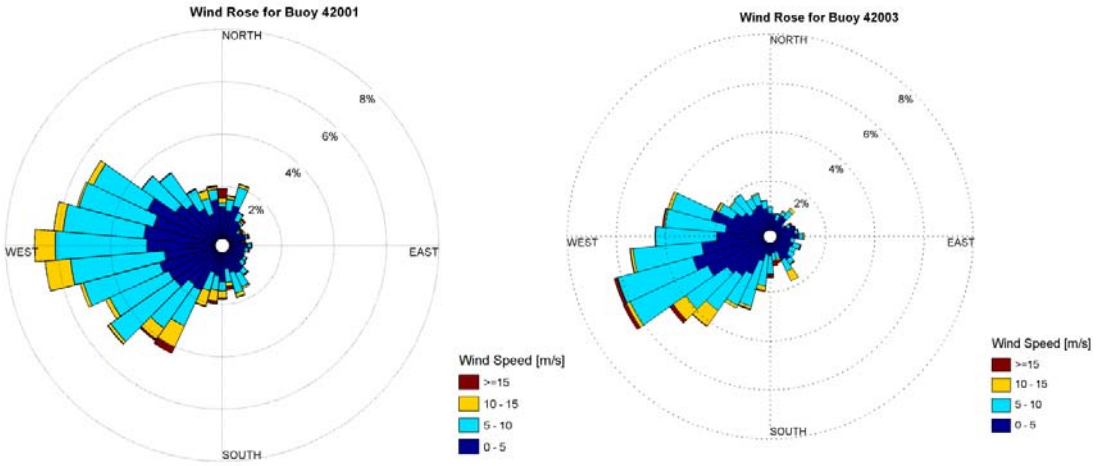

Figure 4-33 Wind Rose for Buoy 42001 (Left) and Buoy 42003 (Right)

In order to see how much the wind could affect the surface current. We listed the wind speeds from two buoys, surface current speeds from the upper most bin of the surface ADCP and the variations of the surface ADCP depths in Fig.4-34. The variations of instrument depths may represent the strength of the whole upper layer currents, since depth variations of the mooring were caused by the strong current. From Fig.4-34, we can see that Katrina induced very strong surface current; however, currents induced by Rita were much weaker (as indicated by the dark blue rectangular). This is because the fact that the mooring was much closer to the track of Katrina than that of Rita as discussed earlier. It is very interesting that during the time periods indicated by the cyan box, there were no strong wind; however, there were very strong currents. The surface currents from Aug. 5th to Aug. 20th were as strong as those during Katrina. We can also identify this strong current from the depths variations of the mooring. It seems that there was a long lasting, very strong current. The only possible answer is the Loop Current. Fig. 4-35 and Fig. 4-36 show the strong currents from ADCP record, while the directions of these currents are generally the same as the directions of the Loop Current, paralleling with the SSH contours, based on the satellite data (indicated by red arrows in Fig. 4-37 and Fig. 4-38). Aside from that, the tight SSH contours in Fig.4-37 and Fig. 4-38 also indicate strong currents based

on quasi-geostrophic flow assumption. There is a 1-4 day time difference between the strongest current and the tightest SSH contours. This may be attributed to the time lag of SSH data, which is discussed before (Section 3.1.3).

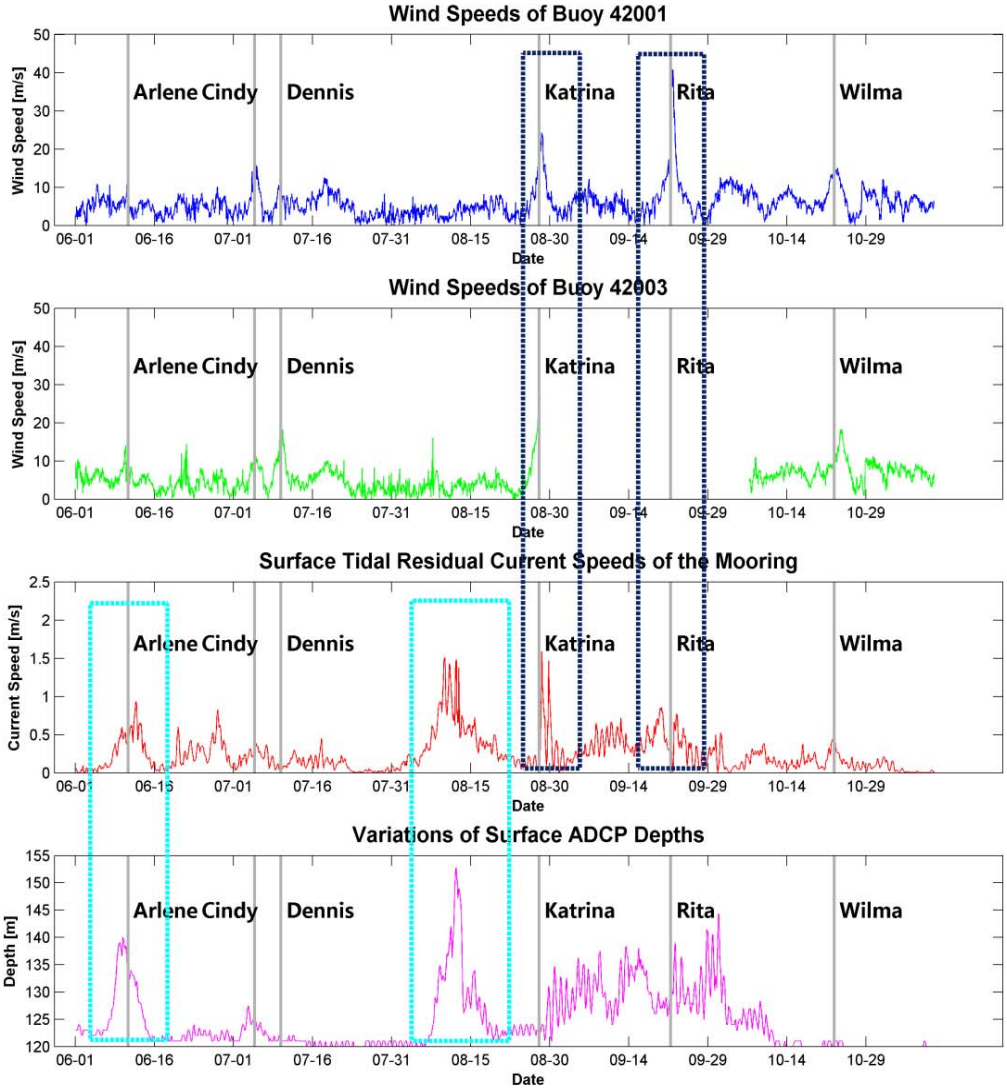

Figure 4-34 Comparison of Wind Speeds, Surface Tidal Residual Current Speeds and Instrument Depth Variations

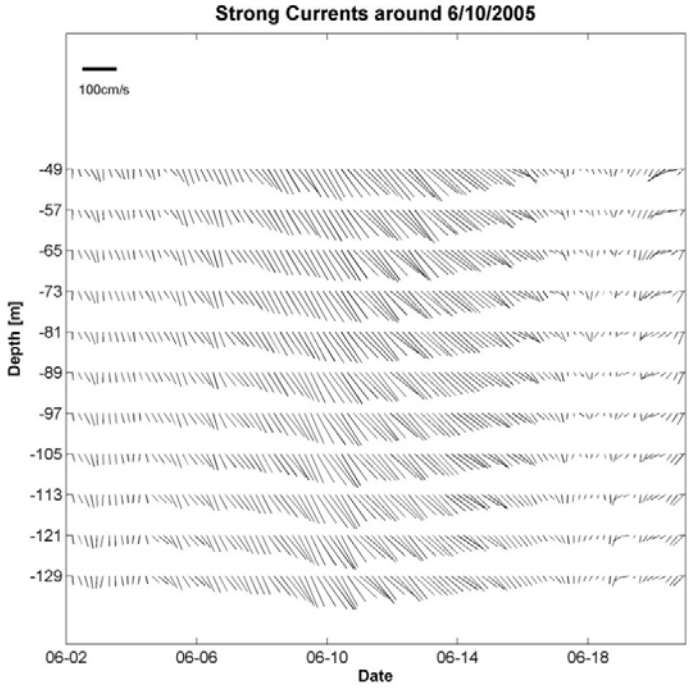

Figure 4-35 Strong Currents around 6/10/2005

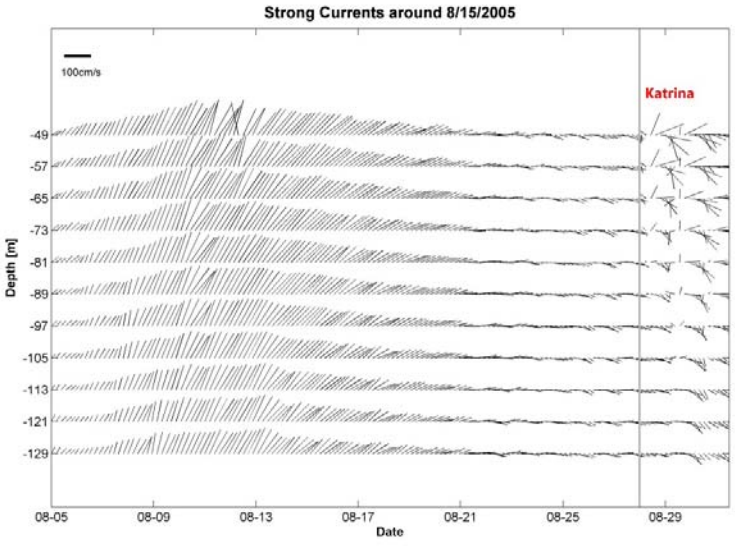

Figure 4-36 Strong Currents around 8/15/2005

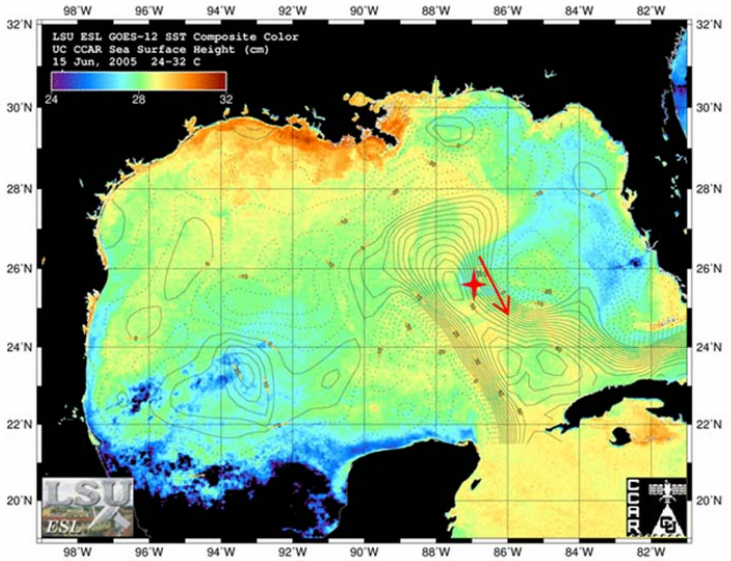

Figure 4-37 SSH contours of 06/15/2005 (The red cross indicates the mooring, while the arrow denotes the current direction based on SSH) (From ESL webpage)

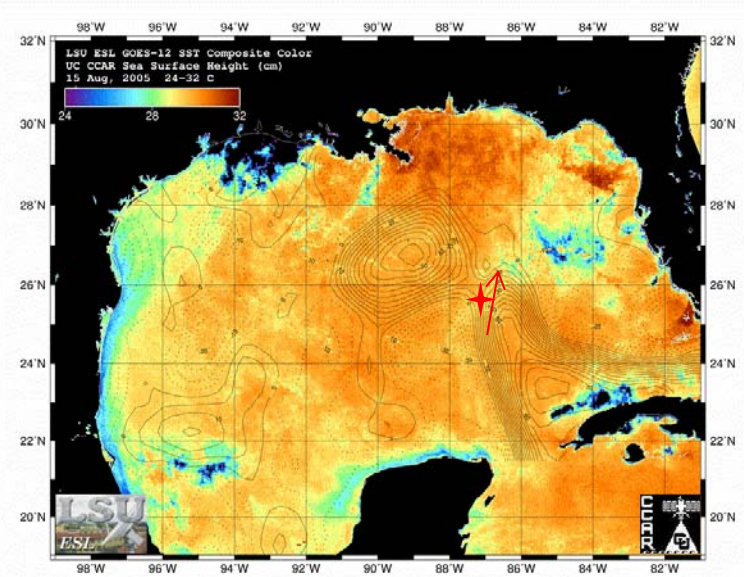

Figure 4-38 SSH contours of 08/15/2005 (The red cross indicates the mooring, while the arrow denotes the current direction based on SSH) (From ESL webpage)

5. Conclusions

In order to better understand the near inertial oscillations caused by hurricanes influenced by local vorticities in Central Gulf of Mexico, data of current, wind and sea surface height from June 1st, 2005 to November 10th, 2005 have been analyzed. This study focuses on the characteristics of near inertial oscillations with respect to energy, frequency and phase, at different depths in response to hurricanes and tropical storms. The primary conclusions are summarized as follows:

For the surface layer, we can identify significant near inertial oscillations during Hurricanes Katrina and Rita. There were also near inertial oscillations in the surface layer during Arlene, Cindy, Dennis and Wilma; however, they were not as clearly associated with these hurricanes or tropical storms (no sudden change in near inertial oscillation strength and no clear time match when hurricanes or tropical storms became closest). The distance between the hurricane center and the mooring is one of the important factors that determines the near inertial oscillation strength. In our case, Hurricane Rita was stronger (Category 5) than Hurricane Katrina (Category 4) when each of them was closest to the mooring, but the near inertial oscillations generated by Katrina were much stronger than those during Rita, because Katrina was much closer to the mooring. Furthermore, comparing the near inertial oscillations during Hurricanes Katrina and Rita, those during Katrina showed a more consistent and long lasting (4-5 local inertial periods) near inertial oscillations, which is demonstrated not only by the consistent near inertial oscillation phases but also by the continuous strong near inertial energy throughout the surface layer, while the large near inertial oscillations in the surface layer during Rita only lasted for 2 local inertial periods and became insignificant for another 2 inertial periods, and showed up again for the next 7 inertial periods. However, we cannot determine whether the latter 7 periods of near inertial oscillations were associated with Rita.

In the rotary spectra of surface currents, most of the time, there is one high peak around local inertial frequency for the clockwise component. If we choose the frequency F corresponding to the highest peak in the rotary spectra as the real near inertial frequency, and compare it with the theoretical near inertial frequency F' suggested by Kunze (1985), the correlation is only 0.3172. The reason may be the time lag of satellite image, the complex local dynamics, the selection of the real near inertial oscillation frequency, the

depth differences between the currents we measured and the satellite indicated and the influence of ageostrophic flows. We also find that these "real" near inertial oscillation frequencies (F) were always higher than the theoretical frequencies (F'), except during Rita.

During Hurricanes Katrina and Rita, there were general coherent phase propagations of the near inertial oscillations from lower layer to upper layer. The phase propagation speed along the vertical in the surface layer was 0.56cm/s during Katrina and 2cm/s during Rita. There were also disturbances in the general regular phase propagations. These disturbances were always accompanied by weak near inertial oscillations. They may represent the propagations of higher frequency internal waves.

In the mid-layer, only during Katrina did we observe significant hurricane induced near inertial oscillations. The downward propagations of near inertial oscillation energy during Katrina can be clearly identified from surface layer to mid-layer. The energy seems to be reflected and refracted by the stratified water column in the mooring area (Welsh et al., 2009). The near inertial energy decayed with depth exponentially, which can be described by the function: Energy=1.19*exp(0.012*Depth). The downward propagation speed varies within each stratified layers (0.047cm/s from 49m-200m depths; 0.25cm/s from 200m to 800m depth and 0.038cm/s from 800 to 1200m depth; no significant propagation below 1200m depth).

In contrast to the slow downward propagations of near inertial oscillations within the surface and mid-layer trough baroclinical processes, the near inertial oscillations in the bottom layer respond to Katrina through barotropical process occurred almost immediately. In addition, the strength of strong Loop Current is comparable to that of severe hurricane induced currents, while the strong Loop Current can last longer than hurricane induced currents. The distance between the hurricane track and the observation position is one of the most important facts in determining the strength of the near inertial oscillations. Future study can include higher temporal and spatial resolution SSH data whenever available (that we do not have for this study) to examine if it is possible to obtain an improved correlation between the real and theoretical frequency of near inertial oscillations when the satellite technology and satellite data quality improve.

References

1. Alford, M. H., Lien, R. C., Simmons, H., Klymak, J., Ramp, S., Yang, Y. J., and Chang, M. H. (2010). Speed and evolution of nonlinear internal waves transiting the South China Sea. *Journal of Physical Oceanography*, *40*(6), 1338-1355.

2. Alford, M. H., Cronin, M. F., & Klymak, J. M. (2012). Annual cycle and depth penetration of wind-generated near-inertial internal waves at Ocean Station Papa in the northeast Pacific. *Journal of Physical Oceanography*, *42*(6), 889-909.

3. Alford, M. H. (2008). Observations of parametric subharmonic instability of the diurnal internal tide in the South China Sea. *Geophysical Research Letters*,*35*(15), L15602.

4. Balmforth, N. J., & Young, W. R. (1999). Radiative damping of near-inertial oscillations in the mixed layer. *Journal of marine research*, *57*(4), 561-584.

5. Chavanne, C. P., Firing, E., & Ascani, F. (2012). Inertial Oscillations in Geostrophic Flow: Is the Inertial Frequency Shifted by ζ/2 or by ζ?. *Journal of Physical Oceanography*, *42*(5), 884-888.

6. Decker, B. L. (1986). *World geodetic system 1984*. Defense Mapping Agency Aerospace Center St Louis Afs Mo.

7. Eckart, C. (1961). Internal waves in the ocean. *Physics of Fluids*, *4*(7), 791.

8. Elipot, S., Lumpkin, R., & Prieto, G. (2010). Modification of inertial oscillations by the mesoscale eddy field. *Journal of Geophysical Research*, *115*(C9), C09010.

9. ESL webpage. (2013). http://www.esl.lsu.edu/imagery/GVAR/goes-gom-sst/latest/

10. Emery, W. J., & Thomson, R. E. (2001). *Data analysis methods in physical oceanography*. Elsevier.

11. Fu, L. L. (1981). Observations and models of inertial waves in the deep ocean.*Reviews of Geophysics*, *19*(1), 141-170.

12. Garrett, C. (2001). What is the “near-inertial” band and why is it different from the rest of the internal wave spectrum?. *Journal of physical oceanography*,*31*(4), 962-971.

13. Gill, A. E. (1984). On the behavior of internal waves in the wakes of storms.*Journal of Physical Oceanography*, *14*(7), 1129-1151.

14. Gill, A. E. (1982). *Atmosphere-ocean dynamics* (Vol. 30). Academic press.

15. Google Maps. (2013) .https://maps.google.com/.

16. Gore, R. H. (1992). "The Gulf of Mexico." *Pineapple, Sarasota, Florida*.

17. Hung, C. C., Gong, G. C., Chung, W. C., Kuo, W. T., & Lin, F. C. (2009). Enhancement of particulate organic carbon export flux induced by atmospheric forcing in the subtropical oligotrophic northwest Pacific Ocean. *Marine Chemistry*, *113*(1), 19-24.

18. Kundu, P. K., & Thomson, R. E. (1985). Inertial oscillations due to a moving front. *Journal of physical oceanography*, *15*(8), 1076-1084.

19. Kunze, E. (1985). Near-inertial wave propagation in geostrophic shear. *Journal of Physical Oceanography*, *15*(5), 544-565.

20. Meinen, C. S. (2008). Accuracy in mooring motion temperature corrections.*Journal of Atmospheric and Oceanic Technology*, *25*(12), 2293-2303.

21. Meyers, P. (2008). Mixed Layer Response to a Hurricane.

22. Munk, W. (1981). Internal waves and small-scale processes. *Evolution of physical oceanography*, 264-291.

23. O'Brien, J. J., & Pillsbury, R. D. (1974). Rotary Wind Spectra in a Sea Breeze Regime. *Journal of applied meteorology*, *13*, 820-824.

24. Oey, L. Y. and Wang. D. P. (2009). Modeling waves and currents produced by Hurricanes Katrina, Rita, and Wilma. U.S. Dept. of the Interior, Minerals Management Service, Herndon, Virginia. *OCS Study MMS* 2009-060. xviii + 135 pp.

25. Pinkel, R. (1984). Doppler sonar observations of internal waves: The wavenumber-frequency spectrum. *Journal of physical oceanography*, *14*(8), 1249-1270.

26. Pinkel, R. (2008). The wavenumber-frequency spectrum of vortical and internal-wave shear in the western Arctic Ocean. *Journal of Physical Oceanography*,*38*(2), 277-290.

27. Shay, L. K., & Elsberry, R. L. (1987). Near-inertial ocean current response to Hurricane Frederic. *Journal of Physical Oceanography*, *17*(8), 1249-1269.

28. Robert, Leben. (2013). Personal Communication.

29. Shearman, R. K. (2005). Observations of near‐inertial current variability on the New England shelf. *Journal of Geophysical Research: Oceans (1978–2012)*,*110*(C2).

30. Sun, L., Zheng, Q., Wang, D., Hu, J., Tai, C. K., & Sun, Z. (2011). A case study of near-inertial oscillation in the South China Sea using mooring observations and satellite altimeter data. *Journal of oceanography*, *67*(6), 677-687.

31. Shcherbina, A. Y., Talley, L. D., Firing, E., & Hacker, P. (2003). Near-surface frontal zone trapping and deep upward propagation of internal wave energy in the Japan/East Sea. *Journal of physical oceanography*, *33*(4), 900-912.

32. Stockwell, R. G., Large, W. G., & Milliff, R. F. (2004). Resonant inertial oscillations in moored buoy ocean surface winds. *Tellus A*, *56*(5), 536-547.

33. Sun, O. M., & Pinkel, R. (2012). Energy transfer from high-shear, low-frequency internal waves to high-frequency waves near Kaena Ridge, Hawaii. *Journal of Physical Oceanography*, *42*(9), 1524-1547.

34. Vanderhoff, J. C., Nomura, K. K., Rottman, J. W., & Macaskill, C. (2008). Doppler spreading of internal gravity waves by an inertia-wave packet. *Journal of geophysical research*, *113*(C5), C05018.

35. Van Meurs, P. (1998). Interactions between Near-Inertial Mixed Layer Currents and the Mesoscale: The Importance of Spatial Variabilities in the Vorticity Field*. *Journal of physical oceanography*, *28*(7), 1363-1388.

36. Wang, D. P. (1991). Generation and propagation of inertial waves in the subtropical front. *Journal of marine research*, *49*(4), 619-633.

37. Welsh, S. E., Inoue, M., Rouse, L.J. and Weeks, E. (2009). Observation of the Deepwater Manifestation of the Loop Current and Loop Current Rings in the Eastern Gulf of Mexico. *OCS Study MMS*, 50. 110pp.

38. Young, W. R., & Jelloul, M. B. (1997). Propagation of near-inertial oscillations through a geostrophic flow. *Journal of marine research*, *55*(4), 735-766.

39. Young, W. R., Tsang, Y. K., & Balmforth, N. J. (2008). Near-inertial parametric subharmonic instability. *Journal of Fluid Mechanics*, *607*, 25-50.

40. Zhai, X., Greatbatch, R. J., & Zhao, J. (2005). Enhanced vertical propagation of storm‐induced near‐inertial energy in an eddying ocean channel model.*Geophysical research letters*, *32*(18).

Vita

Fan Zhang was born in October, 1989, in Dafeng County, Jiangsu Province, China. He graduated from Yancheng High School in 2007. Fan Zhang attended Nanjing University in September, 2007, and obtained a degree of Bachelor of Science in Geography in May, 2007. He was influenced and encouraged by his undergraduate advisor, Dr. Yaping Wang, to pursue his interest and career in oceanography and marine sciences.

Fan entered the graduate program and has been working as a research assistant with Dr. Chunyan Li in the Department of Oceanography and Coastal Sciences at Louisiana State University since August, 2011. He plans to pursue a Doctor of Philosophy degree in University of Maryland, starting from fall, 2013.